Preservation and distribution of detrital clay coats in a modern estuarine heterolithic point bar in the Gironde estuary (Bordeaux, France)

Maxime Virolle, Benjamin Brigaud, Hugues Féniès, Raphaël Bourillot, Eric Portier, Patricia Patrier, Hervé Derriennic, Daniel Beaufort

Preservation and distribution of detrital clay coats in a modern estuarine heterolithic point bar in the Gironde estuary (France)

Maxime Virolle[1], Benjamin Brigaud[1], Hugues Féniès[2], Raphaël Bourillot[2], Eric Portier[1,3], Patricia Patrier[4], Hervé Derriennic[5], Daniel Beaufort[4]

[1]Université Paris-Saclay, CNRS, GEOPS, 91405 Orsay, France
[2]Géoressources et Environnement, ENSEGID, Bordeaux INP, Université Bordeaux Montaigne 33607 Pessac, France
[3]CV Associés Engineering, 7 chemin de la Marouette, 64100 Bayonne, France
[4]Université de Poitiers, CNRS, UMR 7285 IC2MP, 86073 Poitiers Cedex 9, France
[5]Université Bordeaux, CNRS, UMR 5805 EPOC, 33615 Pessac Cedex, France

Corresponding author: benjamin.brigaud@universite-paris-saclay.fr

ABSTRACT

Estuaries provide an excellent depositional environment to study the interaction between minerals (clays, quartz sands…) and biofilms. The estuary bottom is largely covered by biofilms that impact sediment stability, the mud and clay-coat content in sands, and sedimentary-structure stability, thus influencing sandstone properties during burial. Although numerous oil, gas, and geothermal reservoirs are exploited in estuarine heterolithic point bars, many questions remain about the origin of reservoir properties and heterogeneities in these sedimentary bodies. In order to better understand the sedimentary and microbiologic processes in estuarine systems and to better predict the reservoir quality of estuarine sandstones, this study characterizes a modern heterolithic point bar located in the Garonne estuarine channel at various scales, ranging from the microscopic (thin section)

to the macroscopic (core) scale. Three piston cores 4.5 to 6.8 m long were drilled in the Bordeaux North Point Bar. Three main facies were identified in these cores: (1) sandy gravel; (2) heterolithic, medium-grained sand dunes; and (3) thin heterolithic, fine-grained sand beds with mud drapes. The sands are classified as lithic arkoses to feldspathic litharenites. Detrital clay grain coats, which at deep burial depths are transformed to permeability preserving authigenic chlorite coatings, are observed from the base to the top of the point bar. These detrital clay grain coats are mainly composed of smectite, illite, kaolinite, and chlorite, intermixed with other components, such as diatoms or pyrite. Biofilms of exopolymeric substances (EPSs), mostly produced by diatoms, are believed to control the adhesion of the clay coats to the surface of sand grains. Quantification by thin section shows that on average; about 30% of the sands are coated in the point bar. The proportion of clay-coated grains appears to be independent of facies. Radiocarbon age dating measured on organic matter point to significant vertical mixing, highlighting the significance of erosion and redeposition. The activities of ^{137}Cs and ^{210}Pb indicate a vertical sedimentation rate of *ca*. 0.02 $m.yr^{-1}$ in the muddy chute channel. These ages, coupled to historical maps, suggest that the present-day point bar has developed over the last 300 years with a vertical sedimentation rate ranging from 0.015 to 0.036 $m.y^{-1}$ and a lateral migration rate of about 1 $m.y^{-1}$. The combination of sedimentary geology, thin-section petrography, and mineralogy at high spatial and temporal resolutions highlights the potential of this study area as a modern analogue for ancient tidally influenced point-bar deposits associated with clay coatings.

Key words: Facies, Sand, Clay coats, Estuary, Point bar, Gironde, Reservoir analogue, Petrography

INTRODUCTION

Estuaries provide an excellent depositional environment to study the interaction between minerals (clay coating, quartz sands…) and biofilms, mostly produced by diatoms (Smith and Underwood, 1998; Decho, 2000; Wooldridge et al., 2017a; Virolle et al., 2019a; Duteil et al., 2020). Estuarine biofilms consist of exopolymeric substances (EPSs), composed of polysaccharides, proteins, lipids, and nucleic acids, and reactive groups, such as carboxyl or sulfate (Stoodley et al., 2002; Braissant et al., 2007; Duteil et al., 2020). The reactive groups in EPSs formed in shallow marine and coastal environments adhere to mineral surfaces (e.g., clays and sands; Duteil et al., 2020), changing the properties of sediments (Malarkey et al., 2015) and also adsorbing metals (Decho, 2000; Pace et al., 2018). The estuary bottom is largely covered by biofilms that influence sediment stability (Decho, 2000; Malarkey et al., 2015; Shchepetkina et al., 2017, 2018). Biofilms and their EPSs may also play a significant role in Precambrian stratigraphy and sedimentary environmental interpretations, influencing both sediment stability and sedimentary-structure stability (Decho, 2000; Sarkar et al., 2005; Malarkey et al., 2015; Shchepetkina et al., 2017, 2018). EPS is believed to support attachment of organisms to the mud sediment and as a protective cocoon to shelter the organisms against desiccation and erosion (Decho, 2000). Many studies show that tidally influenced point-bar deposits form moderate- to high-quality reservoirs (Martinius et al., 2005; Finotello et al., 2018). Common internal depositional features in point-bar reservoirs are lateral-accretion surfaces and associated bedding features that create intermediate-scale heterogeneities (Jordan and Pryor, 1992; Pranter et al., 2007; Cosma et al., 2019; La Croix et al., 2019). Although porosity and permeability in sandstone reservoirs, including tidally influenced point bars in estuaries, could be damaged by quartz overgrowth, it is widely accepted that authigenic clay chlorite coatings help inhibit quartz cement and preserve deep-reservoir quality (Ehrenberg, 1993; Bloch et al., 2002; Worden and Morad,

2003; Saïag et al., 2016; Worden et al., 2020). Recently, clay coats have been documented in modern shallow-marine deposits of estuaries and estuarine channels (Wooldridge et al., 2017b; Griffiths et al., 2018, 2019b, 2019a; Virolle et al., 2019a). These coats appear to have formed by thermally driven transformations of clay-mineral precursors (Aagaard et al., 2000; Haile et al., 2015; Worden et al., 2020). In modern estuarine environments, clay minerals are found in the sediment during or just shortly after deposition, and EPS appears to play an important role in binding detrital clay to sands (Dowey et al., 2017; Jones, 2017; Griffiths et al., 2019b; Wooldridge et al., 2019a; Virolle et al., 2019a; Duteil et al., 2020). These initial detrital clay minerals are believed to initiate chloritization by promoting the formation of clay-mineral precursors (e.g., berthierine) (Beaufort et al., 2015; Virolle et al., 2019b; Worden et al., 2020). Recent studies of modern analogues such as the Ravenglass (United Kingdom), Gironde (France) and Petitcodiac (Canada) estuaries show that tidal bars in the inner estuary and tidal marshes contain well developed detrital clay coats (Shchepetkina et al., 2017, 2018; Griffiths et al., 2018; Wooldridge et al., 2019a; Virolle et al., 2020).

However, few studies have focused on documenting the grain-size distribution, mineralogy, presence, and distribution of clay coats in point bars deposited in the estuarine channels up to the fluvial–estuarine transition zone, except for studies on the Ogeechee River (USA) (Shchepetkina et al., 2016a), the Petitcodiac River Estuary (Shchepetkina et al., 2017, 2018), the channel parts of the Ravenglass estuary (Griffiths et al., 2018, 2019b, 2019a) and the Garonne estuarine channel, located in the upstream part of the Gironde estuary (Virolle et al., 2019a). To date, no study has evaluated the influence of point-bar architecture on clay-coat distribution. Therefore, comprehensive models of detrital-clay coating processes, distribution, preservation, and heterogeneity in these challenging heterolithic point bars are still needed.

This study focused on the modern Bordeaux North heterolithic point bar, located in the Garonne estuarine channel (SW France). The objective was to characterize the point-bar heterogeneity from large-scale (i.e., hundreds of meters) to microscale and to discuss the factors potentially influencing clay-grain-coat occurrences and reservoir potential. This primary goal of this study is to provide a better understanding of the distribution and prediction of porosity and permeability in deeply buried tidally influenced sandstone reservoirs.

GEOLOGICAL SETTING

The Gironde estuary (Nouvelle Aquitaine; southwestern France) is one of the largest estuaries in Europe with a surface area of 630 km^2 (Sottolichio et al., 2011) (Fig. 1A). The estuary is divided into three morphological zones: (1) the Garonne and Dordogne estuarine (meandering) channels, characterized by the deposition of sandy heterolithic point bars; (2) the inner estuary funnel, where the tidal bars of the bay-head delta are deposited; and (3) the outer estuary funnel, consisting in a wide muddy central basin with tidal bars and a large tidal inlet channel at its seaward extremity (Fig. 1A; Allen, 1991; Allen and Posamentier, 1993; Féniès and Tastet, 1998; Billy et al., 2012; Chaumillon et al., 2013; Virolle et al., 2020). The Bordeaux North point bar is located in the Garonne estuarine channel. It is a sinuous single channel, 85 km long, which extends inland from the landward extremity of the estuary funnel to the upstream tidal limit located 160 km from the estuary mouth (Fig. 1A). It is characterized by its low gradient and narrow channel (about 500 m at Bordeaux). Several point bars are observed along the meanders. These point bars are heterolithic and are composed of fluvial sand dunes and amalgamated slack-water mud drapes (Allen, 1991; Virolle et al., 2019a). The Bordeaux North point bar is located 94 km upstream from the

123 estuary mouth, north of the city of Bordeaux. It is about 1100 m long and 200 m wide (Fig.
124 1B, C). It has been deposited in the lower part of the intertidal zone, including the entire
125 subtidal zone, down to the thalweg of the channel. The intertidal part of the point bar is
126 covered by (1) a network of small dunes, which can be observed from the low-tide limit to
127 the crest of the bar, and (2) a muddy chute channel, around 100 m wide, located between
128 the crest of the point bar and the channel bank. The channel banks are composed of a 3-m-
129 thick section of muddy estuarine coastal-plain sediments that were deposited up to the
130 high-tide limit. The Garonne river's discharge rate varies seasonally, reaching the highest
131 values in January–February and the lowest in August–September (Coynel et al., 2004). The
132 Gironde is well known for its well-developed Turbidity Maximum Zone (TMZ). In the TMZ,
133 concentration of suspended particle matter (SPM) is reported to be a few $g.l^{-1}$ in surface
134 waters, but in the fluid mud zone (FMZ) near the estuary bottom, the concentration of fine
135 particles (< 4 μm) can reach 100 300 $g.l^{-1}$ (Castaing and Allen, 1981; Sottolichio et al., 2011;
136 Etcheber et al., 2011). Jalon-Rojas et al. (2015) reported that the TMZ today in the Garonne
137 channel near Bordeaux seems independent of salinity and density currents.
138
139 **MATERIAL AND METHODS**
140 This study is mainly based on a new set of shallow piston cores (Fig. 1). Coring was
141 conducted along an east–west transect perpendicular to the long axis of the bar, which has
142 developed almost parallel to the direction of tidal currents. Three cores were drilled in 2016
143 and 2017 in the heterolithic point bar: 1) Bo-2016-E at the east; 2) Bo-2016-W at the west;
144 and 3) Bo-2017-C in the center of the cross section (Fig. 1C). The length of the cores varies
145 from 4.44 m to 6.70 m. Core spacing is about 60 m (Fig. 1B, C). A portable vibro-corer was
146 used to recover these cores (De Resseguier, 1983) (Fig. 2). During coring, the core barrel is

147 hammered without any rotation. A fixed piston is maintained with a cable in order to
148 prevent deformation and fluidization due to water escape, thus preserving the delicate
149 sedimentary structures. A reference line indicating the ebb direction of the tide is marked
150 along the entire core section to facilitate orientation of the dune bedding (ebb and flood)
151 after core extraction in the field.
152 Forty-three plugs (diameter 4 cm) were sampled from the cores. Thin sections of epoxy-
153 impregnated sediment samples were observed under a Nikon Eclipse Ci-POL (Nikon, Tokyo,
154 Japan) and a Leica DM 750P (Leica Microsystems, Wetzlar, Germany) polarizing microscope.
155 Since "clay" may refer to both grain size and mineralogy, this study uses the term “clay
156 fraction” to define the < 2 µm fine-grained sediment (Grim, 1942). In each thin section, the
157 relative surface area (%) of macroporosity and the sediment composition (coated and non-
158 coated quartz grains, feldspars, lithics, pyrite, bioclasts, micas, and clay matrix) were
159 quantified using random grid point counting with JmicroVision Image analysis software
160 (Roduit, 2007). Five grain classes were identified (following the classification defined by
161 Wooldridge et al. (2019b)): (1) absence of clay coats; (2) 1–5% of the grain surface coated;
162 (3) 5–15% of the grain surface coated; (4) 15–30% of the grain surface coated; and (5) more
163 than 30% of the grain surface coated. Scanning electron microscope (SEM) observations,
164 coupled with energy dispersive X-ray spectrometry (EDS), were made on individual sand
165 grains with a Phenom X Pro SEM (Phenom-World B.V., Eindhoven, Netherlands). Cryo–
166 scanning electron microscopy (cryo-SEM) analyses were also conducted on select samples to
167 document EPS and clay minerals attached to the sand grains. Grain size was determined on
168 78 samples using a Mastersizer 2000 laser granulometer (Malvern, Worcestershire, UK).
169

The relative weight percentage of the clay fraction of homogenized sediment subsamples was also measured on 78 samples. It was expressed as a weight percentage of the sample (wt.%). The compositions of the clay fraction (< 2 µm) were determined by X-ray diffraction (XRD) using a PANalytical X'Pert Pro X-ray diffractometer (PANalytical, Almelo, Netherlands). Samples analyzed by XRD analyses included modern mud pebbles in dunes, clay drapes and coats. Semiquantitative estimates of clay minerals (smectite, illite, kaolinite, and chlorite) were made using Macdiff software. These were based on the peak area of the ethylene-glycol diffractograms summed to 100% (the relative error for the peak area is ±5%) (Petschick, 2002).

Short-wavelength infrared (SWIR) spectroscopy was performed on 318 core samples (103 from Bo-2016-E and 215 from Bo-2016-W). Samples for SWIR were collected every 2 cm.

Macroscopic fragments of organic matter (wood, leaves, or seed debris) were sampled for radiocarbon dating. The age dating on 27 samples was made using the mass spectrometer accelerator at the Adam Mickiewicz University in Poznań (Poland) and at Paris-Saclay University (Gif-sur-Yvette, France). In all, 228 dried sediment samples from the top 130 cm of core Bo-2016-W were analyzed in 2017 for ^{210}Pb, ^{226}Ra, and ^{137}Cs by direct gamma assay at the Environmental Radioactivity Laboratory at the University of Liverpool (England) using an Ortec HPGe GWL series well-type coaxial-low background intrinsic germanium detector (Appleby et al., 1986). Isotope ^{210}Pb was identified from its gamma emissions at 46.5 keV, and ^{226}Ra by the 295 keV and 352 keV gamma rays emitted by its daughter isotope ^{214}Pb (after three weeks of storage in sealed containers to allow for radioactive equilibration). Isotope ^{137}Cs was measured at 662 keV. Unsupported ^{210}Pb activities were calculated by subtracting ^{226}Ra activity from total ^{210}Pb activity. The absolute efficiencies of the detectors were determined using calibrated sources and sediment samples of known activity. Eight

Corrections were made for the effect of self-absorption of the low energy gamma rays within the sample (Appleby et al., 1992).

Appendix 1 contains the raw XRD values obtained for the clay fraction and raw Image Analysis data on the framework mineralogy of each sample.

RESULTS

Facies Characterization of the Heterolithic Point Bar

Table 1 summarizes the facies descriptions for each point-bar core (from the bottom to top). The sandstones range from lithic arkose to feldspathic arkose (Classification of Folk, 1974) with an average grain composition of quartz (37%), feldspars (11%), lithics (wood debris, soft mud clasts) (14%), carbonates (3%), clays (17%), and micas (5%) (Table 2, Fig. 3A). The average mean grain size in the point-bar deposits is 223 μm. The vertical grain-size profiles show an overall fining-upward trend, ranging from pebbles and coarse-grained sands at the base of the bar (facies F1) to fine-grained sands and mud at the top of the point bar (facies F3). These three facies form the dominant vertical facies association, with F1 at the base to F3 at the top of the heterolithic point bar (Fig. 2). The heterolithic point bar has further been divided into (1) lower point bar (deeper than 3 m below the low water of spring tides), composed mainly of facies F1 and F2, (2) upper point bar, composed mainly of facies F2 and F3, and (3) chute channel deposits composed of the clayey facies F3 only. High resolution photographs of cores are available in Appendices 2, 3, and 4.

Facies F1: Sandy Gravels

Observations: Facies F1 is composed of pluri-centimetric to pluri-decimetric beds of coarse-grained sands, gravels, and lithics (soft mud clasts and organic fragments (wood)), which are

bounded by basal erosional surfaces. No sedimentary structures are visible. Locally, horizons rich in organic matter are observed, composed mainly of wood debris, leaves, and seeds. In the channel thalweg at the base of the core, Bo-2016-W, this facies is composed entirely of pebbles (Fig. 4).

Interpretation: The coarse-grained deposits of facies F1 are believed to have been deposited during floods stage, when current velocities are highest, whereas the organic-matter debris was deposited during waning flood currents. The pebble bed observed at the base of core Bo-2016-W is interpreted as the upper part of a channel lag deposit.

Facies F2: Heterolithic medium-grained sand dunes

Observations: Facies F2 is heterolithic. It is made up of decimeter-thick beds of sand dunes, interbedded with centimeter- to decimeter-thick muddy beds. The sand beds are composed of small- to medium-size dunes (preserved dune set height: 10–30 cm). Their foresets and bottomsets are underlined by mud pebbles and mud drapes. The mud pebbles are subrounded and centimeters thick; mud drapes are a few millimeters thick on the foresets, but up to half a centimeter thick in the bottomsets of the dunes, where they appear to be amalgamated (Fig. 2). Mud-drape couplets (Visser, 1980; Féniès et al., 1999) are preserved in the dune foresets and bottomsets. The bidirectionality of tidal currents can be observed at the dune scale with: (i) flood- and ebb-oriented tidal bundles on dune foresets; and (ii) reactivation surfaces (De Mowbray and Visser, 1984) generated by the subordinate currents, which have eroded the dominant current bundle. Muddy beds are composed of amalgamated millimeter to centimeter-thick individual mud drapes. No bioturbation was observed.

Interpretation: The internal stratification of the sand dunes proves that they were deposited by bidirectional tidal currents, whose velocities exceeded the dune migration threshold. The mud drapes were deposited during slack-water periods in very turbid waters. The apparent lack of bioturbation is typical for estuarine high-turbidity fresh-water estuarine deposits (La Croix et al., 2015).

- **Facies F3: Heterolithic fine-grained sands beds and mud drapes**

Observations: Facies F3 is heterolithic and consists of thin fine-grained sand beds (mostly ripples and linsen), interbedded with centimeter-thick mud layers composed of amalgamated, millimeter-thick individual mud drapes. This facies is characterized by its classic lenticular bedding. Neap-spring-cycle deposits (Boersma and Terwindt, 1981) a few decimeters thick have also been described. The spring-tide deposits consist of centimeter-thick, fine-grained sandy ripples interbedded with thin mud drapes. The neap tide deposits consist of fine-grained silty linsen interbedded with thicker mud drapes. These deposits have been previously described by Musial et al. (2012).

A subfacies of facies F3 is the chute channel deposits, which are located on the western side of the point bar, between the crest of the point bar and the estuarine bank (see core Bo-2016-W location in Fig. 1C and Fig. 2). The chute channel deposits are 3 m thick (Fig. 4). They are characterized by alternating beds of fluid mud (centimeters to decimeters thick) and beds of fine-grained thin sand ripples, linsen, and mud drapes (decimeters thick). A few beds of coarse-grained sand and pebbles (centimeters thick) are occasionally observed.

Rare bioturbation was observed on the surfaces of the mud drapes, generated by millimetric-size small horizontal burrowing worms.

Interpretation: The ripples and linsen were deposited by tidal currents, whose velocities only just exceeded the ripple migration threshold. The thick mud drapes were deposited in highly turbid waters, during long slack-water periods. The preservation of neap-spring-cycle deposits indicates a very high rate of sedimentation with sufficient accommodation space.

The subfacies F3 chute-channel deposits are representative: (1) periods of very low current velocities during which the fluid mud layers were deposited, or (2) periods of very high current velocities, attained during high flood stage, resulting in the deposit of coarse-grained sand and pebbles beds [were deposited] in the chute channel. The crypto-bioturbation present at the surface of the chute channel is typical of estuarine high-turbidity fresh-water estuaries.

- **Facies F4: Admixed sand and mud facies**

Observations: Facies F4 was encountered only in core Bo-2016-E, from the surface of the point bar to a depth of 235 cm (Table 1, Fig. 4). It is a mixture of mud and sand, characterized by very disturbed bedding with a lot of brick and shipyard bolts debris.

Interpretation: Facies F4 is made up of anthropized dredging deposits. This facies is confined to a small area on the western side of the point bar.

Contribution of Radiometric Age Datings

- **^{14}C Datings**

Twenty-one ^{14}C dates were obtained on the three cores (Bo-2016-W; Bo-2017-C; Bo-2016-E). Results revealed very heterogeneous ages, ranging from 6,280 years before present (BP) to the present (Fig. 4). Except for two ages older than 1,000 years BP, the predominant ages in

the upper part of the tidal bar (between 0 and 4.5 m below the low-water spring-tide level (LWST)) are younger than 400 years BP.

- **^{210}Pb Activity**

The results of ^{210}Pb analyses conducted on core Bo-2016-W are given in Table 3 and figure 5A. Total ^{210}Pb activity significantly exceeds that of the supporting ^{226}Ra in samples down to a depth of around 90 cm. Unsupported ^{210}Pb concentrations are very low, with a maximum value of just 38 Bq kg^{-1}. The total ^{210}Pb activity exhibits some variation with depth. Between the surface and 50 cm depth, the total activity fluctuates between 45 and 80 Bq kg^{-1}. From 50 to 110 cm deep, it decreases steadily from 70 to 20 Bq kg^{-1} before stabilizing around 40 Bq kg^{-1} between 110 cm and 140 cm deep (Fig. 5A).

- **^{137}Cs Activity**

The ^{137}Cs analyses obtained from core Bo-2016-W is around 6000 Bq m^{-2}. ^{137}Cs activity in this core has a well-defined peak at a depth of 28 cm (Table 3, Fig. 5A), reaching a maximum value of 8.4 Bq kg^{-1}. Between 28 to 110 cm, activity fluctuates between 4 and 6 Bq kg^{-1}. A last peak at 5.7 Bq kg^{-1} is observed at 108 cm depth, before it decreases to almost 0 Bq kg^{-1} from 116 to 234 cm deep (Table 3). Between the surface sample and 28 cm deep, ^{137}Cs activity ranges from almost 2 to more than 8 Bq kg^{-1}.

Characterization of Detrital-Clay Grain Coat

Detrital-clay grain coats are present throughout the heterolithic point bar (down to *ca*. 7 m deep). Clay grain coats were observed around various framework grains (quartz, micas, feldspars, and lithics, except the Channel lag facies F1; Figs. 3B-G). The detrital-clay grain

311 coats are mainly composed of clay minerals with minor amounts of silt-size quartz grains,
312 coccoliths, diatoms, and framboidal pyrite (Fig. 3F-H). Both optical microscopy and SEM
313 observations show that diatoms are embedded in the detrital clay grain coats from the
314 surface to several meters below the tops of the cores (Figs. 6A-E).
315 Various textures were observed, ranging from (1) continuous to discontinuous clay drapes, 5
316 to 50 µm thick, partially to totally cover the surface of the detrital grains (Fig. 3E); (2)
317 aggregates of detrital-clay coats in aggregates scattered on the surface of sand grains (Figs.
318 3D, 3F); (3) detrital-clay bridges between sand grains (Fig. 3C); to (4) detrital-clay ridges
319 where the clay minerals are oriented at high angles to the surfaces of detrital sand grains.
320 The detrital-clay grain coats are typically less than 1 millimeter thick, ranging mainly from 10
321 to several hundred µm. All these clay coat textures were observed in all facies (Fig. 3).
322 Detrital sand grains on average represent 70% of the sample composition, and 31% of the
323 grains are coated (Table 2, Fig. 7). Vertically, the total number of coated grains ranges from
324 19% to 48% (Table 2; Fig. 8). In each facies, the coated grain-content is very homogeneous:
325 sandy gravel facies (F1) = 29%; heterolithic, medium-grained sand dune facies (F2) = 31%,
326 and heterolithic, fine-grained sand bed and mud drape facies (F3) = 32% (Fig. 7, Table 2).
327 Coat coverage is relatively homogeneous for all cores (Fig. 9). For the finer sand of the
328 heterolithic facies (F3), the two predominant classes of clay grain-coat-coverage are 5–15%
329 and 15–30%. In facies F1 and F2, more than 20% of the grain are coated, with a coverage
330 ranging from 1 to 15% (Fig. 7). Overall, there is no correlation between clay fraction and the
331 percentage of coated grain (Fig. 9A, B).
332
333 *Characterizations of Clay Fractions and Clay Assemblages*

334 The clay fraction is related to the amount of muddy deposits (muddy layers or clay drapes)
335 and coats in a sample. On average, the total clay content makes up about 20 wt.% of the
336 sample (Table 2; Figs 8, 9B). In facies F1 and F2, the amount of clay is very consistent (18%),
337 but it is slightly higher in facies F3 (25%) (Fig. 9B). The muddy chute-channel subfacies (F3)
338 has a higher clay content (38 wt.%), as shown in Figs. 8 and 9B (Table 2). It should be noted
339 that the clay-fraction content in facies F3 might be slightly underestimated because of bias
340 in sample selection (most of the samples were extracted from sandy ripples).
341 Based on XRD analysis, the clay-mineral assemblage is composed of four main clay minerals:
342 chlorite, illite, kaolinite, and smectite (Fig. 10, Table 2). Chlorite is characterized by
343 diffraction peaks at 14.10 Å (001), 7.05 Å (002), 4.73 Å (003), and 3.54 Å (004). The illite
344 diffraction pattern exhibits diffraction peaks around 9.99 Å (001), 4.99 Å (002), and 3.33 Å
345 (003). Kaolinite displays a (001) diffraction peak at 7.16 Å and a (002) diffraction peak at 3.57
346 Å. Smectite is identifiable after ethylene-glycol saturation, with a (001) diffraction peak close
347 to 17 Å. Smectite is mainly dioctahedral smectite (Latouche, 1971). Smectite (7%) and illite
348 (8%) have the highest surface areas (on the diffractogram), while chlorite and kaolinite have
349 a much lower surface area (average of 2%; Fig. 9C-F, Table 2). Clay assemblages are relatively
350 homogeneous between facies, except for facies F3 in core Bo-2016-W (the muddy chute-
351 channel subfacies) where the abundance of all clay minerals is systematically higher:
352 smectite (14%), illite (16%), kaolinite (4%), and chlorite (3%) (Fig. 9C-F).
353 Short-wavelength infrared (SWIR) measurements were made along cores Bo-2016-W and
354 Bo-2016-E. Of particular interest were three bands: (1) the water-absorption band, which
355 can be correlated with the presence of swelling minerals such as smectite, and (2) the 2200
356 cm^{-1} (Al_2OH) and 2253 cm^{-1} bands, both of which mainly characterize aluminous phases, such
357 as micas or clay minerals. In core Bo-2016-E, none of the bands show significant variation

with depth or even between facies in core Bo-2016-E (Fig. 8). In core Bo-2016-W, each of the three bands displays a slightly increasing trend with depth, coupled with higher fluctuations (Fig. 8).

DISCUSSION

Age Model of Cores

Previous studies have used ^{137}Cs–^{210}Pb chronologies to reconstruct the morphological evolution of point-bar deposits through time (D'Alpaos et al., 2017). In montmorillonite, vermiculite, kaolinite, and illite, the isotope ^{137}Cs is essentially fixed on particles of permanent charge due to cationic exchange on the mineral compounds (Grousset et al., 1999). The isotope ^{137}Cs is mostly incorporated into the illitic clay matrix of the Gironde suspended matter and is therefore difficult to desorb. This is why it was relevant to carry out ^{137}Cs–^{210}Pb dating in the muddy deposits of the chute channel enriched in smectite (montmorillonite) and illite (Fig. 5A). Calibrations were made by comparisons with Grousset et al. (1999) and Jouanneau et al. (1999), who studied a core located 3 km upstream in the flood-tide dock of Bordeaux (Fig. 1B).

The atmospheric initiation of radioactive fallout since 1952 is responsible for the increase in ^{137}Cs activity in sediments, reaching a ^{137}Cs peak in 1964 (e.g., Monna et al., 1999; Evrard et al., 2020). The beginning of this increase can be seen at *ca.* 124 cm with a small ^{137}Cs peak at 0.4 Bq kg^{-1} (Fig. 5A, B). The peak of ^{137}Cs activity at 5.7 Bq kg^{-1} recorded at 108 cm below the top of core could correspond to the year 1964, which was marked by the maximum impact of nuclear tests in the northern hemisphere (Pourchet et al., 1989; Williams and Hamilton, 1995; Jouanneau et al., 1999; Monna et al., 1999) (Fig. 5A, B). This increase in ^{137}Cs activity from the mid-1950s to 1964, also corresponds to an increase in cadmium (Cd) in the estuary,

suggesting an increase in river inputs (Grousset et al., 1999; Jouanneau et al., 1999). In the Bordeaux dock core, ^{137}Cs reaches a maximum at 3 dpm g^{-1} (50 Bq kg^{-1}) for 1964 (Jouanneau et al., 1999), whereas ^{137}Cs reaches 120 Bq kg^{-1} in Lake Geneva (Switzerland) for the same year (Monna et al., 1999). The presence of small but significant concentrations of ^{137}Cs down to a depth of 110 cm suggests that all sediments above this depth postdate the large-scale release of this artificial radionuclide into the global environment from the mid-1950s onwards (Fig. 5A-B). This is consistent with the suggestion that the greatest depth (~90 cm) at which significant amounts of unsupported ^{210}Pb could be detected was likely to span at most 2–3 ^{210}Pb half-lives (40–60 years). According to the age model of the core from the dock of Bordeaux, a second ^{137}Cs peak occurs in the 1970s (Grousset et al., 1999). The peak found at 84 cm (5.7 Bq kg^{-1}) in core Bo-2016-W (Fig. 5A-B) could also correspond to this event.

The third ^{137}Cs peak (ca. 20 Bq kg^{-1}) recognized in the Bordeaux dock core corresponds to the Chernobyl accident that occurred in 1986 (Grousset et al., 1999). The third peak (6.5 Bq kg^{-}1) is also found 60 cm deep in core Bo-2016-W (Fig. 5A-B). The fourth ^{137}Cs peak (8.4 Bq kg^{-1}) found at 28 cm is not attributed to a known discharge, source or event. The temporal evolution of ^{210}Pb element is characterized by great variability in the upper part of the chute channel between 20 and 30 cm, possibly suggesting sediment remobilization (Fig. 5A).

Placing year 1964 at 108 cm and 1986 at 60 cm, the average sedimentation rate can be estimated to be *ca*. 2 cm.y^{-1} (Fig. 5C). The results from ^{210}Pb total activity are consistent with ^{137}Cs activity, as the first 110 centimeters of the core would be less than 60 years old (Fig. 5A, B). By anchoring years 1964 at 108 cm and 1986 at 60 cm, and applying a sedimentation rate of 2 cm y^{-1}, the sample at 12 cm which contains significantly higher concentrations of

405 uranium-series radionuclides appears to have been deposited to around 2010. The samples
406 at 26–28 cm contained the highest ^{137}Cs concentration, suggesting that they were deposited
407 around 2002.

408 Radiocarbon ages dating was performed on the three cores at all depths. These ages are
409 very heterogeneous, ranging from 6280 ± 30 years BP to modern (Fig. 4). Results may
410 depend on the nature of organic remains. Fine organic debris, such as leaves and twigs, are
411 assumed to record ages close to the age of sediment deposition (because they are
412 seasonally produced and readily decomposed (Kochel and Baker, 1988; Webb et al., 1988)
413 and therefore are believed to yield the most accurate ^{14}C dates in fluvial deposits (Ely et al.,
414 1992). Detrital wood and charcoal ^{14}C ages may predate fluvial deposits by centuries after
415 sedimentation and can be remobilized giving erroneous ages of deposition (Long and
416 Rippeteau, 1974; Blong and Gillespie, 1978; Ely et al., 1992). In the Bordeaux North point
417 bar, radiocarbon ages measured on seeds and leaf debris are younger than 400 years (Fig. 4).
418 The top 110 cm of the well-calibrated core Bo-2016-W, yielded two ^{14}C ages (modern and
419 195 ± 30 years BP). This suggests that the youngest age obtained provides information about
420 sediment age. Older ^{14}C ages suggest that old organic matter has been remobilized and
421 transported into the estuary (Virolle et al., 2020). In core Bo-2016-W, an age of 70 ± 30 years
422 BP was obtained at a depth of 3.1 m (in the upper section of the point bar) (Fig. 4),
423 suggesting that the top 3 m is relatively young, probably deposited during the last century.
424 This suggests a sedimentation rate of *ca*. 3 cm y^{-1}. In core Bo-2016-W, an age of 355 ± 30
425 years BP at a depth of 5.3 m suggests that the sedimentation rate for the top 5 m was
426 around 1.5 cm y^{-1}. In core Bo-2017-C, leaf fragments at a depth of 3.2 m yielded an age of
427 170 ± 20 years BP at the top of the lower point bar (Fig. 4). This age suggests that the top
428 3 m was also relatively young, probably deposited in the two last centuries, and

corresponding to a sedimentation rate of *ca*. 1.9 cm y^{-1}. In core Bo-2016-E, the age 95 ± 30 years BP in the lower point bar (depth of 3.4 m) (Fig. 4) suggests a sedimentation rate of 3.6 cm y^{-1} in the upper point bar. A recent study reports that the sedimentation rate is about 1–3 $mm.y^{-1}$ in a tidal point bar of the lagoon of Venice (Donnici et al., 2017). The sedimentation rate in the Bordeaux point bar is higher by a factor of ten.

Radiometric ages (^{14}C, ^{137}Cs, and ^{210}Pb) suggest that the formation of the Bordeaux North point bar is relatively young and rapid (< 300 years). This is consistent with lateral migration studies which document that the point bar has migrated about 200 m since the period 1820–1866, yielding a lateral-accretion rate of 1 $m.y^{-1}$ (Fig. 11). In comparison, detailed studies of the tidal point bars of the Venice Lagoon show lateral-accretion rates of only 0.1 to 0.25$m.y^{-1}$ (Donnici et al., 2017; D'Alpaos et al., 2017; Ghinassi et al., 2018).

Origin of Detrital-Clay Grain Coats

Grain coats observed in the Gironde estuary are mainly composed of clay minerals (Fig. 6). As described in Virolle et al. (2019a), these clay minerals are detrital and supplied by the Garonne and Dordogne rivers. These two rivers are responsible for 70% and 18%, respectively, of the supply of detrital clay minerals to the estuary funnel respectively (Latouche, 1971; Parra et al., 1998). The seasonal position of the turbidity-maximum zone (TMZ) seems to be a major factor controlling the amount of clay, the clay-mineral assemblage, and the coated-grain distribution, in the intertidal zone of the estuary (Virolle et al., 2019a).

The incorporation of clay particles in the heterolithic point-bar deposits seems to be mostly related to hydrodynamic variations (seasonal variations in river discharge associated with seasonal TMZ position and tidal-current cycles), rather than mechanical infiltration or

453 bioturbation processes, as bioturbation is rarely observed and no significant variations in
454 clay content are observed in near-surface sediments (Virolle et al., 2019a). If these
455 postdepositional (mechanical infiltration or bioturbation) processes occurred, they are minor
456 and do not overprint the distribution of detrital-clay grain coats in surface sediments or in
457 the vertical facies associations of the point bar.
458 Diatom biofilms extensively cover the chute channel, especially during the summer (Virolle
459 et al., 2019a). These biofilms produce abundant exopolymeric substances (EPSs), especially
460 on the surface of the chute channel (facies F3, Virolle et al., 2019a). The role of EPSs in
461 binding detrital clay to sand grains has been discussed in several modern estuarine studies
462 (Shchepetkina et al., 2017, 2018; Jones, 2017; Wooldridge et al., 2017a; Virolle et al., 2019a).
463 EPSs produced by biofilms observed in the chute channel, could be resuspended during a
464 semidiurnal cycle (Underwood and Kromkamp, 1999) and transported in suspension, finally
465 interacting with sand grains and clay particles on the surface of the point bar. This
466 interaction could result in the formation of clay-coated sand grains in the zone of deposition
467 of facies F2 (Fig. 12). Aggregates of detrital-clay grain coats in facies (F1), are observed only
468 in depressions or hollows of detrital grains. As these grains are transported by rolling during
469 periods of strong currents or flood events, these coats would be expected to be preserved
470 only in depressions. It also supposes that these coats are probably inherited, preserved, and
471 formed in another location of the point bar or facies before being incorporated in facies (F2
472 or F3) after sediment transport. Verhagen et al. (2020) demonstrated experimentally that
473 clay coats can be preserved during sediment transport in turbulent flows of about 50 $cm.s^{-1}$.
474 This velocity is reached during all tidal cycles in the point bar and corresponds to the
475 formation of dunes in Facies F1. The high clay fraction (> 30% in sandy beds) in the muddy
476 facies of core Bo-2016-W (muddy chute-channel facies) could be due to the *in situ*

production of EPS and clay entrapment by diatom biofilms (Figs 6A, B, 12; Virolle et al., 2019a). The presence of the chute channel and the mud-rich F3 facies appears to be a key point required for the production of biofilms and on the coated grains in the point bars. The chute channel traps both mud and clay (a favorable location for biofilm development), and thus appears to play an important role in binding clay to sand grains in the point bar.

Clay-Coat Composition and Mineralogy in a Modern Point Bar

The detrital-clay grain coats observed in cores are consistent with those reported in surface sediments, in the intertidal zone of the heterolithic point bar (Virolle et al., 2019a). Infrared measurements (at a very tight sampling step) provide rapid and continuous information about the clay content of the core (Fig. 8). Overall, they confirm the relative stability of clay mineralogy with depth. A focus on certain adsorption bands, such as the water band (at about 1900 nm) or the bands characteristic of aluminous phases (at 2200 and 2253 nm) reveals local accumulations of smectite or mica (Fig. 8). Locally, in core Bo-2016-W, each band exhibits a slightly increasing trend coupled with stronger fluctuations with depth (between 4 and 6 m deep) (Fig. 8). Since the clay content does not particularly increase downward, this could be due to the overall increase in the mica content. Petrographically, similar textures are observed (ridged, aggregated, or bridged textures) at all core depths. XRD analyses confirm a homogeneous clay-mineral composition in the tidal bar: (1) illite represents on average 9 wt.% of the total sediment and 45% of the clay content; (2) smectite represents on average 7 wt.% of the total sediment and 34% of the clay content; (3) chlorite represents on average 1.8 wt.% of the total sediment and 9% of the clay content; and (4) kaolinite represents on average 2.4 wt.% of the total sediment and 12% of clay content. Occasional silt-size quartz, carbonates, and pyrite are also observed embedded in detrital-

clay grain coats (Fig. 3G). The clay assemblage and the associated minerals are comparable to those reported from the Plassac tidal bar, which is located 30 km downstream in the Gironde inner estuary funnel (Virolle et al., 2019a, 2020). In contrast, the clay-mineral assemblage differs from the Richard tidal bar, which is located 70 km downstream in the Gironde outer estuary funnel. The Richard tidal-bar sediments contain less smectite (3 wt.%) and more illite (16 wt.%) (Virolle et al., 2019a, 2020).

In the alluvial plain of the Ravenglass estuary, the average clay content of 15% is slightly lower (Griffiths et al., 2019) than the 20% clay content found in the Bordeaux north point bar (20%). The majority of sand grain surfaces of the Ravenglass estuarine channels are covered by clay coats, with coat coverage greater than 30% (Griffiths et al., 2018, 2019a). The main difference in the clay-mineral assemblage is the absence of smectite (Griffiths et al., 2018, 2019a), with illite being the main clay mineral in 1–6 wt.% of the samples and representing 60% of the clay content. As in the Bordeaux North point bar, only minor amounts of kaolinite and illite (0.01–3%) were found, confirming that the Garonne estuarine channel is more turbid than the Ravenglass estuary (Griffiths et al., 2019).

Reservoir Implications

Authigenic chlorite coats have been recognized to play a significant role in preserving porosity in sandstones around the world (Pittman and Lumsden, 1968; Thomson, 1979; Ehrenberg, 1993; Bloch et al., 2002; Anjos et al., 2003; Taylor et al., 2010; Ajdukiewicz and Larese, 2012; Sun et al., 2014; Huggett et al., 2015; Saïag et al., 2016; Virolle et al., 2019b; Worden et al., 2020). Sandstones where at least 60-80% of the grains were coated (Virolle et al., 2019b; Worden et al., 2020) and/or at least 80% of quartz surfaces are covered by clay coats (Lander and Walderhaug, 1999; Taylor et al., 2010; Stricker et al., 2016) have been

found to have the best reservoir quality. Numerical models for quartz cementation suggest that complete grain coats are needed to preserve porosity in deep, high-temperature (> 70-80 deg C) reservoirs (Bloch et al., 2002; Lander et al., 2008). Modern studies have found that from 2 to 10% chlorite is needed to fully coat quartz grains (Virolle et al., 2019b; Worden et al., 2020). At all scales, in the Garonne Bordeaux North heterolithic point bar, the facies with the least mud baffles were found to be the sand-dominated facies (F1 and F2) (Figs. 3, 4, 6; Table 2). On average, in these two facies, medium-grained sandstone (mean grain size of 292 µm) were typically composed of 30% clay-coated grains, with about 5-15% of the quartz grain surfaces covered in clay, a chlorite clay content of about 2%, and a total clay fraction of 20 wt.% (Tables 1, 2, Figs. 4, 12). The clay fraction of Facies F3 was typically higher (25%) and contained a higher amount of coated grains (32%) (Table 2, Fig. 8). Those values are significantly lower the 60-80% values and 80% quartz surface coverage proposed in the literature for chloritized reservoirs (Lander and Walderhaug, 1999; Taylor et al., 2010; Stricker et al., 2016; Virolle et al., 2019b; Worden et al., 2020). This difference is mainly due to the diagenetic process of recrystallization from detrital-clay coats to authigenic chlorite. It has been proposed that authigenic grain-coating chlorite, especially Fe-rich chlorite, does not form directly from solution by precipitation during eogenesis (Beaufort et al., 2015) but through a complex chloritization processes that involves the formation of an Fe-rich clay-mineral precursor, such as berthierine (Hornibrook and Longstaffe, 1996; Beaufort et al., 2015; Virolle et al., 2019b; Worden et al., 2020). During the chloritization process, the detrital-clay coatings initially covering 30% of the sand grains and 5-15% of the quartz grain surfaces are homogeneously redistributed around grains. After chloritization, it is likely that the percentage of coated grains in the sediment increases from 30% initially to more than 80%. It is also likely that the coat coverage (coat surface) around the detrital quartz grains

549 increases from an initial 5-15% to > 80%, almost complete coat coverage. From a diagenetic
550 perspective, the detrital-clay grain coats composed of kaolinite, illite, smectite, and chlorite
551 found in the Bordeaux North heterolithic point bar might evolve into chlorite coatings during
552 eogenesis and burial diagenesis, and the initiation of chloritization actually begins with the
553 formation of an early clay-mineral precursors, such as berthierine (Gould et al., 2010;
554 Beaufort et al., 2015; Worden et al., 2020) that eventually with increasing temperature and
555 pressure evolve into chlorite grain coats that inhibit the development of quartz cement and
556 thus preserve deep-reservoir quality. Facies F1 and F2 have the best reservoir potential if
557 deeply buried (more 2.5 km). We consider that the initial coated-grain content (about 30%)
558 and initial clay-fraction content of the sediment (on average lower than 20 wt.%) could be
559 conducive to the preservation of a porosity network (Fig. 12). In the interbedded sands of
560 facies F3, 20-35% of clays could potentially stop development of quartz overgrowths and
561 minimize porosity loss during burial diagenesis. However, it is likely that higher clay contents
562 favor the development of pore-filling clay, rather than fine clay coatings, thus resulting in the
563 loss of porosity during burial. Lastly, this study found that the mud-rich facies F3 and the
564 chute channel facies are favorable to the development of biofilms and may play an
565 important role in the binding of clay to sand grains in the heterolithic point bar.
566 Comparisons between modern analogues (such as the Garonne estuarine heterolithic point
567 bars) and deeply buried reservoirs are key to improving predications of reservoir quality in
568 deeply buried estuarine heterolithic point-bar reservoirs (Martinius et al., 2005) by providing
569 critical information on the initial conditions necessary for the crystallization of chlorites
570 during burial (Byrne et al., 2011; Shchepetkina et al., 2016b, 2018; Wooldridge et al., 2017b,
571 2019a; Dowey et al., 2017; Griffiths et al., 2019b, 2019a; Virolle et al., 2019a, 2020; Worden
572 et al., 2020). The next step will be to fully understand the conditions of incipient

chloritization in shallow buried sediments (temperature, depth, pressure, chemical conditions), especially the role of iron reduction in promoting the development of chlorite precursors (such as berthierine)

CONCLUSION

(1) ^{14}C dating suggests that the Bordeaux North point bar has settled over the last 300 years. ^{137}Cs and ^{210}Pb chronologies highlight that the sedimentation rate in the chute channel is about 2 $cm.y^{-1}$. ^{14}C ages suggesting that the average vertical sedimentation rate ranged from 1.5 to 3.6 $cm.y^{-1}$ in the point bar. Radiometric ages (^{14}C, ^{137}Cs, and ^{210}Pb), coupled with historical data found that the point bar has migrated laterally, approximately 200 m to the northeast since 1820, suggesting a lateral migration rate of 1 $m.y^{-1}$.

(2) The Garonne point bar is composed of three main facies: (1) sandy gravels; (2) heterolithic, medium-grained sand dunes; and (3) heterolithic, fine-grained sand beds and mud drapes. Sands are classified as lithic arkoses to feldspathic litharenites. The coated-grain content, coat coverage, or the mineralogy of the coats and distribution is not controlled by facies.

(3) Clay coats were observed in the entire vertical sequence of a heterolithic point bars in the modern Gironde estuarine channel (at depths down to almost 7 m). The clay assemblage is composed on average of (1) 9% illite, (2) 7% smectite, (3) 2% chlorite, and (4) 2% kaolinite. Detrital-clay grain coats, generally less than 1 mm thick (10 to several hundred µm), were observed on fine- to-medium-grained sands (average grain size *ca*. 223 µm). In the chute channel facies, EPSs produced by diatoms were identified that may interact directly with detrital grains. In the suspended particulate

matter of the tidal channel, EPSs could play a key role in binding clay particles around sand grains during the saltation or rolling of sand grains.

(4) On average, 31% of detrital sand grains are coated, covering 5 to 15% of the total grain surface area. These early coatings could initiate chloritization during burial diagenesis, by transforming into clay precursors (such as berthierine), thus promoting the preservation of reservoir quality by inhibiting quartz overgrowths.

ACKNOWLEDGMENTS

This work is the result of collaborative project No P04980 CLAYCOAT "CLAY COATing in shallow marine clastic deposits to improve reservoir quality prediction" between Paris-Saclay University, Bordeaux INP, Bordeaux Montaigne University, University of Poitiers, and Neptune Energy. This study has benefitted greatly from Engie and Neptune Energy funding. The authors would also like to thank Julius Nouet (Paris-Saclay University) and Thibault Duteil (Bordeaux INP) for assistance with SEM observations. We thank Anne-Sophie Canivet and Marie-Charlotte Geffray for their help with the granulometry analyses and Nicolas Saspitury (Bordeaux INP) for his help with coring of Bordeaux North point bar. We are grateful to Léa Pigot (Bordeaux INP) and Valérie Godard (Paris-Saclay University) for the high-quality thin sections. We also thank the "Sediment Archive Analysis" Platform at the EPOC laboratory (Bordeaux, France) with Isabelle Billy, Pascal Lebleu, and Olivier Ther. Marc Massault from GEOPS (Paris-Saclay University) is to be thanked for their assistance with graphite preparation and with ^{14}C counting at Gif-sur-Yvette using the energy accelerator mass spectrometer (AMS) "ECHoMICADAS - Environnement Climat et Homme Micro Carbon Dating System" of Paris-Saclay University. Two anonymous reviewers, Associate Editor

620 Marcia Whitlock French, and Editor Kathleen M. Marsaglia are thanked for their useful and
621 constructive comments that improved an earlier version of this manuscript.
622
623 **FIGURES**
624
625 **Figure 1:** A) Simplified facies map of the Gironde estuary. B) Bathymetric map showing the
626 location of the Bordeaux North point bar. C) Google Earth aerial view of the point bar. Yellow
627 stars indicate the location of the cores sampled in this study: Bo-2016-W, Latitude (°N):
628 44.895911, Longitude (°E): -0.540475; Bo-2017-C, Latitude (°N): 44.896000, Longitude (°E): -
629 0.539836; Bo-2016-E, Latitude (°N): 44.896086, Longitude (°E): -0.539217. The Bordeaux
630 dock core was described in Jouanneau et al. (1999).
631 **Figure 2:** Left: Stratigraphic column showing principal facies of the Bordeaux North
632 heterolithic point bar. Middle: Field photographs showing facies in the intertidal zone of the
633 point bar. Right: Representative core photographs from the three main facies (F1, F2 and
634 F3).
635 **Figure 3:** A) quartz-feldspar-lithic (QFL) ternary diagram (after Folk, (1974) showing the
636 framework composition of Bordeaux North point-bar samples. B) Thin-section
637 photomicrograph of mud drape and sand bed (BORNW-P4, 127 cm, F3). C) Thin-section
638 photomicrograph showing clay-coatings bridges (br.), aggregates (agg.), and clay drapes (dr.)
639 [arrows] around detrital framework grains (BORNW-P17, 590 cm, F3). D) Thin-section
640 photomicrograph of clay-coated detrital grains showing clay-coatings bridges (br.),
641 aggregates (agg.), and clay drapes (dr.) [arrows] (BORNW-P17, 590 cm, F3). E) Thin-section
642 photomicrograph showing clay-coated framework grains in sand dunes, showing clay-
643 coatings bridges (br.), aggregates (agg.), and clay drapes (dr.) [arrows] (BORN2C-P3, 84 cm,

F2). F) SEM image showing clay coatings on a quartz grain from sandy gravel facies [yellow box indicates location of G] (BORNE-P14, 438 cm, F1 facies). G) Close-up view of the clay coat displayed in Part F. The clay coatings are mainly composed of detrital clay minerals and occasional silt-size grains and authigenic pyrite [+ marks location of EDS spot analysis]. H) EDS spectrum of a clay coat on detrital quartz seen in Part G, Spots 1 consists primarily of detrital clay; KEY: Qz = quartz; Li = lithoclast; Fd = feldspar; W = wood debris. See Figure 4 for the location of the thin sections.

Figure 4: E-W stratigraphic cross section across the Bordeaux North point bar showing the three cores analyzed in this study: Bo-2016-W; Bo-2017-C and Bo-2016-E with associated ages. pMC: percent modern carbon (modern age).

Figure 5: A) Vertical profiles showing ^{137}Cs and ^{210}Pb activities along core Bo-2016-W. This part of the core corresponds to facies F3 of the chute channel (see Fig. 4). B) Core photograph of facies F3 and ages obtained after data processing. C) Time (horizontal-axis) vs. depth (vertical-axis) plot constructed using ^{137}Cs and ^{210}Pb activities.

Figure 6: A) Thin-section microphotographs showing diatoms embedded in detrital-clay grain coats in facies F3 from the Bordeaux North point bar (BORNW-P5, 179 cm). B) SEM image showing diatom embedded in detrital-clay grain coats in facies F2 from the Bordeaux North point bar (BORN2C-P3, 84 cm). C, D, E) Cryo-SEM images of sediment sample from the Bordeaux North point bar (depth 25 cm). C) Low-magnification SEM view of quartz sand grain coated with an EPS-clay complex. D) Composite EDS spectra of the two analyzed spots marked with + in Part E. Spot 1 [black line] confirms detrital quartz grain host. Spot 2 appears to be an aluminous phyllosilicate (clay-mineral signature). E) SEM close-up view of Part C showing the alveolar network formed by EPS intermixed with patchy clay platelets. See Figure 4 for the location of samples BORNW-P5 and BORN2C-P3.

Figure 7: Histograms showing average grain-coat content per facies divided into coat coverage classes. The sum of the coat coverage classes gives the total coated-grain content for each facies.

Figure 8: Summary core logs showing evolution with depth of mean grain size, percentage of < 2 µm particles, and relative fraction of clay minerals, coated-grain content, and FTIR measurements for the three cores from the Bordeaux North point bar.

Figure 9: Plots representing the mean proportions in % of A) coated-grain content (from image analysis), B) clay-fraction content (weighted percentage of clay fraction from total volume), C) smectite (from XRD analysis), D) illite (from XRD analysis), E) kaolinite (from XRD analysis), and F) chlorite (from XRD analysis) in each facies. Above each histogram is the number of samples analyzed.

Figure 10: X-Ray diffractograms of the < 2 µm fraction showing dominant clay minerals (BORNW-11, depth: 281 cm). See Fig. 4 for the location of this sample.

Figure 11: Aerial photographs showing lateral bank accretion from 1820–1866 to present of the Bordeaux North point bar (Source: IGN maps, https://remonterletemps.ign.fr).

Figure 12: A) Synthetic diagram of the heterolithic point-bar deposits at macro- (core) and micro- (thin-section) scales. The core drawing illustrates the heterolithic vertical facies association, while the thin-section documents how the clay coats are distributed. B) Cartoon summarizing how detrital-clay coatings may form on a heterolithic point bar. C) Table showing the average clay values, total clay, and grain-coat coverage by facies. KEY: EPS: exopolymeric substances.

REFERENCES

692 Aagaard, P., Jahren, J.S., Harstad, A.O., Nilsen, O., and Ramm, M., 2000, Formation of grain-
693 coating chlorite in sandstones. Laboratory synthesized *vs*. natural occurrences: Clay
694 Minerals, v. 35, p. 261–269, doi:10.1180/000985500546639.

695 Ajdukiewicz, J.M., and Larese, R.E., 2012, How clay grain coats inhibit quartz cement and
696 preserve porosity in deeply buried sandstones: Observations and experiments:
697 American Association of Petroleum Geologists, Bulletin, v. 96, p. 2091–2119,
698 doi:10.1306/02211211075.

699 Allen, G.P., 1991, Sedimentary processes and facies in the Gironde estuary: a recent model
700 for macrotidal estuarine systems, *in* Smith, D.G., Zaitlin, B.A., Reinson, G.E., and
701 Rahmani, R.A. eds., Clastic Tidal Sedimentology, Recognition Criteria and Facies
702 Models, v. Memoir 16, p. 29–39.

703 Allen, G.P., and Posamentier, H.W., 1993, Sequence Stratigraphy and Facies Model of an
704 Incised Valley Fill: The Gironde Estuary, France: Journal of Sedimentary Petrology,
705 v. 63, doi:10.1306/D4267B09-2B26-11D7-8648000102C1865D.

706 Anjos, S.M.C., De Ros, L.F., and Silva, C.M.A., 2003, Chlorite Authigenesis and Porosity
707 Preservation in the Upper Cretaceous Marine Sandstones of the Santos Basin,
708 Offshore Eastern Brazil, *in* Worden, R.H. and Morad, S. eds., Clay Mineral Cements
709 in Sandstones, Oxford, UK, Blackwell Publishing Ltd., p. 289–316,
710 doi:10.1002/9781444304336.ch13.

711 Appleby, P.G., Nolan, P.J., Gifford, D.W., Godfrey, M.J., Oldfield, F., Anderson, N.J., and
712 Battarbee, R.W., 1986, ^{210}Pb dating by low background gamma counting:
713 Hydrobiologia, v. 143, p. 21–27, doi:10.1007/BF00026640.

714 Appleby, P.G., Richardson, N., and Nolan, P.J., 1992, Self-absorption corrections for well-
715 type germanium detectors: Nuclear Instruments and Methods in Physics Research
716 Section B: Beam Interactions with Materials and Atoms, v. 71, p. 228–233,
717 doi:10.1016/0168-583X(92)95328-O.

718 Beaufort, D., Rigault, C., Billon, S., Billault, V., Inoue, A., Inoue, S., and Patrier, P., 2015,
719 Chlorite and chloritization processes through mixed-layer mineral series in low-
720 temperature geological systems – a review: Clay Minerals, v. 50, p. 497–523,
721 doi:10.1180/claymin.2015.050.4.06.

722 Billy, J., Chaumillon, E., Féniès, H., and Poirier, C., 2012, Tidal and fluvial controls on the
723 morphological evolution of a lobate estuarine tidal bar: The Plassac Tidal Bar in the
724 Gironde Estuary (France): Geomorphology, v. 169–170, p. 86–97,
725 doi:10.1016/j.geomorph.2012.04.015.

726 Bloch, S., Lander, R.H., and Bonnell, L., 2002, Anomalously high porosity and permeability
727 in deeply buried sandstone reservoirs: Origin and predictability: American Association
728 of Petroleum Geologists, Bulletin, v. 86, p. 301–328.

729 Blong, R.J., and Gillespie, R., 1978, Fluvially transported charcoal gives erroneous ^{14}C ages
730 for recent deposits: Nature, v. 271, p. 739–741.

731 Boersma, J.R., and Terwindt, J.H.J., 1981, Neap–spring tide sequences of intertidal shoal
732 deposits in a mesotidal estuary: Sedimentology, v. 28, p. 151–170.

733 Braissant, O., Decho, A.W., Dupraz, C., Glunk, C., Przekop, K.M., and Visscher, P.T., 2007,
734 Exopolymeric substances of sulfate-reducing bacteria: Interactions with calcium at
735 alkaline pH and implication for formation of carbonate minerals: Geobiology, v. 5, p.
736 401–411, doi:10.1111/j.1472-4669.2007.00117.x.

737 Byrne, G.M., Worden, R.H., Hodgson, D.M., Polya, D.A., Lythgoe, P.R., Barrie, C.D., and
738 Boyce, A.J., 2011, Understanding the fate of iron in a modern temperate estuary:
739 Leirárvogur, Iceland: Applied Geochemistry, v. 26, p. S16–S19,
740 doi:10.1016/j.apgeochem.2011.03.018.

741 Castaing, P., and Allen, G.P., 1981, Mechanisms controlling seaward escape of suspended
742 sediment from the Gironde: A macrotidal estuary in France: Marine Geology, v. 40, p.
743 101–118, doi:10.1016/0025-3227(81)90045-1.

744 Chaumillon, E., Féniès, H., Billy, J., Breilh, J.-F., and Richetti, H., 2013, Tidal and fluvial
745 controls on the internal architecture and sedimentary facies of a lobate estuarine tidal
746 bar (The Plassac Tidal Bar in the Gironde Estuary, France): Marine Geology, v. 346,
747 p. 58–72, doi:10.1016/j.margeo.2013.07.017.

748 Cosma, M., Ghinassi, M., D'Alpaos, A., Roner, M., Finotello, A., Tommasini, L., and Gatto,
749 R., 2019, Point-bar brink and channel thalweg trajectories depicting interaction
750 between vertical and lateral shifts of microtidal channels in the Venice Lagoon (Italy):
751 Geomorphology, v. 342, p. 37–50, doi:10.1016/j.geomorph.2019.06.009.

752 Coynel, A., Schafer, J., Hurtrez, J., Dumas, J., Etcheber, H., and Blanc, G., 2004, Sampling
753 frequency and accuracy of SPM flux estimates in two contrasted drainage basins:
754 Science of The Total Environment, v. 330, p. 233–247,
755 doi:10.1016/j.scitotenv.2004.04.003.

756 D'Alpaos, A., Ghinassi, M., Finotello, A., Brivio, L., Bellucci, L.G., and Marani, M., 2017,
757 Tidal meander migration and dynamics: A case study from the Venice Lagoon:
758 Marine and Petroleum Geology, v. 87, p. 80–90,
759 doi:10.1016/j.marpetgeo.2017.04.012.

760 De Mowbray, T., and Visser, M.J., 1984, Reactivation surfaces in subtidal channel deposits,
761 Oosterschelde, Southwest Netherlands: Journal of Sedimentary Petrology, v. 54, p.
762 811–824.

763 De Resseguier, A., 1983, A portable coring device for use in the intertidal environment:
764 Marine Geology, v. 52, p. M19–M23, doi:10.1016/0025-3227(83)90015-4.

765 Decho, A.W., 2000, Microbial biofilms in intertidal systems: an overview: Continental Shelf
766 Research, v. 20, p. 1257–1273, doi:10.1016/S0278-4343(00)00022-4.

767 Donnici, S., Madricardo, F., and Serandrei-Barbero, R., 2017, Sedimentation rate and lateral
768 migration of tidal channels in the Lagoon of Venice (Northern Italy): Estuarine,
769 Coastal and Shelf Science, v. 198, p. 354–366, doi:10.1016/j.ecss.2017.02.016.

770 Dowey, P.J., Worden, R.H., Utley, J., and Hodgson, D.M., 2017, Sedimentary controls on
771 modern sand grain coat formation: Sedimentary Geology, v. 353, p. 46–63,
772 doi:10.1016/j.sedgeo.2017.03.001.

773 Duteil, T., Bourillot, R., Grégoire, B., Virolle, M., Brigaud, B., Nouet, J., Braissant, O.,
774 Portier, E., Féniès, H., Patrier, P., Gontier, E., Svahn, I., and Visscher, P.T., 2020,
775 Experimental formation of clay-coated sand grains using diatom biofilm exopolymers:
776 Geology, v. 48, p. 1012–1017, doi:10.1130/G47418.1.

777 Ehrenberg, S.N., 1993, Preservation of anomalously high porosity in deeply buried sandstones
778 by grain-coating chlorite: examples from the Norwegian continental shelf: American
779 Association of Petroleum Geologists, Bulletin, v. 77, p. 1260–1286.

780 Ely, L.L., Webb, R.H., and Enzel, Y., 1992, Accuracy of post-bomb ^{137}Cs and ^{14}C in dating
781 fluvial deposits: Quaternary Research, v. 38, p. 196–204, doi:10.1016/0033-
782 5894(92)90056-O.

783 Etcheber, H., Schmidt, S., Sottolichio, A., Maneux, E., Chabaux, G., Escalier, J.-M.,
784 Wennekes, H., Derriennic, H., Schmeltz, M., Quéméner, L., Repecaud, M., Woerther,
785 P., and Castaing, P., 2011, Monitoring water quality in estuarine environments:
786 lessons from the MAGEST monitoring program in the Gironde fluvial-estuarine
787 system: Hydrology and Earth System Sciences, v. 15, p. 831–840, doi:10.5194/hess-
788 15-831-2011.

789 Evrard, O., Chaboche, P.-A., Ramon, R., Foucher, A., and Laceby, J.P., 2020, A global
790 review of sediment source fingerprinting research incorporating fallout radiocesium
791 (^{137}Cs): Geomorphology, v. 362, p. 107103, doi:10.1016/j.geomorph.2020.107103.

792 Féniès, H., Resseguier, A.D., and Tastet, J., 1999, Intertidal clay-drape couplets (Gironde
793 estuary, France): Sedimentology, v. 46, p. 1–15, doi:10.1046/j.1365-
794 3091.1999.00196.x.

795 Féniès, H., and Tastet, J.-P., 1998, Facies and architecture of an estuarine tidal bar (the
796 Trompeloup bar, Gironde Estuary, SW France): Marine Geology, v. 150, p. 149–169,
797 doi:10.1016/S0025-3227(98)00059-0.

798 Finotello, A., Lanzoni, S., Ghinassi, M., Marani, M., Rinaldo, A., and D'Alpaos, A., 2018,
799 Field migration rates of tidal meanders recapitulate fluvial morphodynamics:
800 Proceedings of the National Academy of Sciences, v. 115, p. 1463–1468,
801 doi:10.1073/pnas.1711330115.

802 Folk, R.L., 1974, Petrology of Sedimentary Rocks: Austin, Texas, Hemphill Publishing
803 Company, v. 182, 184 p.

804 Ghinassi, M., D'alpaos, A., Gasparotto, A., Carniello, L., Brivio, L., Finotello, A., Roner, M.,
805 Franceschinis, E., Realdon, N., Howes, N., and Cantelli, A., 2018, Morphodynamic
806 evolution and stratal architecture of translating tidal point bars: Inferences from the
807 northern Venice Lagoon (Italy) (J. Howell, Ed.): Sedimentology, v. 65, p. 1354–1377,
808 doi:10.1111/sed.12425.

809 Gould, K., Pe-Piper, G., and Piper, D.J.W., 2010, Relationship of diagenetic chlorite rims to
810 depositional facies in Lower Cretaceous reservoir sandstones of the Scotian Basin:
811 Sedimentology, v. 57, p. 587–610, doi:10.1111/j.1365-3091.2009.01106.x.

812 Griffiths, J., Worden, R.H., Wooldridge, L.J., Utley, J.E.P., and Duller, R.A., 2019a,
813 Compositional variation in modern estuarine sands: Predicting major controls on

814 sandstone reservoir quality: American Association of Petroleum Geologists, Bulletin,
815 v. 103, p. 797–833, doi:10.1306/09181818025.

816 Griffiths, J., Worden, R.H., Wooldridge, L.J., Utley, J.E.P., and Duller, R.A., 2018, Detrital
817 Clay Coats, Clay Minerals, and Pyrite: A Modern Shallow-Core Analogue For
818 Ancient and Deeply Buried Estuarine Sandstones: Journal of Sedimentary Research, v.
819 88, p. 1205–1237, doi:10.2110/jsr.2018.56.

820 Griffiths, J., Worden, R.H., Wooldridge, L.J., Utley, J.E.P., Duller, R.A., and Edge, R.L.,
821 2019b, Estuarine clay mineral distribution: Modern analogue for ancient sandstone
822 reservoir quality prediction: Sedimentology, v. 66, p. 2011–2047,
823 doi:10.1111/sed.12571.

824 Grim, R.E., 1942, Modern Concepts of Clay Materials: The Journal of Geology, v. 50, p.
825 225–275, doi:10.1086/625050.

826 Grousset, F.E., Jouanneau, J.M., Castaing, P., Lavaux, G., and Latouche, C., 1999, A 70 year
827 Record of Contamination from Industrial Activity Along the Garonne River and its
828 Tributaries (SW France): Estuarine, Coastal and Shelf Science, v. 48, p. 401–414,
829 doi:10.1006/ecss.1998.0435.

830 Haile, B.G., Hellevang, H., Aagaard, P., and Jahren, J., 2015, Experimental nucleation and
831 growth of smectite and chlorite coatings on clean feldspar and quartz grain surfaces:
832 Marine and Petroleum Geology, v. 68, p. 664–674,
833 doi:10.1016/j.marpetgeo.2015.02.006.

834 Hornibrook, E.R.C., and Longstaffe, F.J., 1996, Berthierine from the Lower Cretaceous
835 Clearwater Formation, Alberta, Canada: Clays and Clay Minerals, v. 44, p. 1–21,
836 doi:10.1346/CCMN.1996.0440101.

837 Huggett, J.M., Burley, S.D., Longstaffe, F.J., Saha, S., and Oates, M.J., 2015, The nature and
838 origin of authigenic chlorite and related cements in Oligo-Miocene reservoir
839 Sandstones, Tapti Gas Fields, Surat Depression, Offshore Western India: Journal of
840 Petroleum Geology, v. 38, p. 383–409, doi:10.1111/jpg.12618.

841 Jalón-Rojas, I., Schmidt, S., and Sottolichio, A., 2015, Turbidity in the fluvial Gironde
842 Estuary (southwest France) based on 10-year continuous monitoring: sensitivity to
843 hydrological conditions: Hydrology and Earth System Sciences, v. 19, p. 2805–2819,
844 doi:10.5194/hess-19-2805-2015.

845 Jones, S., 2017, Goo, glue, and grain binding: Importance of biofilms for diagenesis in
846 sandstones: Geology, v. 45, p. 959–960, doi:10.1130/focus102017.1.

847 Jordan, D.W., and Pryor, W.A., 1992, Hierarchical Levels of Heterogeneity in a Mississippi
848 River Meander Belt and Application to Reservoir Systems: Geologic Note (1):
849 American Association of Petroleum Geologists, Bulletin, v. 76,
850 doi:10.1306/BDFF8A6A-1718-11D7-8645000102C1865D.

851 Jouanneau, J.-M., Castaing, P., Grousset, F., Buat-Ménard, P., and Pedemay, P., 1999,
852 Enregistrement sédimentaire et chronologie (^{137}Cs) d'une contamination en cadmium
853 dans l'estuaire de la Gironde (France): Comptes Rendus de l'Académie des Sciences -
854 Series IIA - Earth and Planetary Science, v. 329, p. 265–270, doi:10.1016/S1251-

855 8050(99)80245-6.

856 Kochel, R.C., and Baker, V., 1988, Paleoflood analysis using slackwater deposits, *in* Baker,
857 V., Kochel, R.C., and Patton, P.C. eds., Flood Geomorphology, Wiley-Interscience, p.
858 357–376.

859 La Croix, A.D., Dashtgard, S.E., Gingras, M.K., Hauck, T.E., and MacEachern, J.A., 2015,
860 Bioturbation trends across the freshwater to brackish-water transition in rivers:
861 Palaeogeography, Palaeoclimatology, Palaeoecology, v. 440, p. 66–77,
862 doi:10.1016/j.palaeo.2015.08.030.

863 La Croix, A.D., Dashtgard, S.E., and MacEachern, J.A., 2019, Using a modern analogue to
864 interpret depositional position in ancient fluvial-tidal channels: Example from the
865 McMurray Formation, Canada: Geoscience Frontiers, v. 10, p. 2219–2238,
866 doi:10.1016/j.gsf.2019.03.008.

867 Lander, R.H., Larese, R.E., and Bonnell, L.M., 2008, Toward more accurate quartz cement
868 models: The importance of euhedral versus noneuhedral growth rates: American
869 Association of Petroleum Geologists, Bulletin, v. 92, p. 1537–1563,
870 doi:10.1306/07160808037.

871 Lander, R.H., and Walderhaug, O., 1999, Predicting Porosity through Simulating Sandstone
872 Compaction and Quartz Cementation: American Association of Petroleum Geologists,
873 Bulletin, v. 83, p. 433–449, doi:10.1306/00AA9BC4-1730-11D7-
874 8645000102C1865D.

875 Latouche, C., 1971, Les argiles des bassins alluvionnaires aquitains et des dépendances
876 océaniques: contribution à l'étude d'un environnement [Thèse de doctorat, Université
877 de Bordeaux]: Institut de Geologie du Bassin d'Aquitaine, 415 p.

878 Long, A., and Rippeteau, B., 1974, Testing Contemporaneity and Averaging Radiocarbon
879 Dates: American Antiquity, v. 39, p. 205–215, doi:10.2307/279583.

880 Malarkey, J., Baas, J.H., Hope, J.A., Aspden, R.J., Parsons, D.R., Peakall, J., Paterson, D.M.,
881 Schindler, R.J., Ye, L., Lichtman, I.D., Bass, S.J., Davies, A.G., Manning, A.J., and
882 Thorne, P.D., 2015, The pervasive role of biological cohesion in bedform
883 development: Nature Communications, v. 6, p. 6257, doi:10.1038/ncomms7257.

884 Martinius, A.W., Ringrose, P.S., Brostrøm, C., Elfenbein, C., Næss, A., and Ringås, J.E.,
885 2005, Reservoir challenges of heterolithic tidal sandstone reservoirs in the Halten
886 Terrace, mid-Norway: Petroleum Geoscience, v. 11, p. 3–16, doi:10.1144/1354-
887 079304-629.

888 Monna, F., Dominik, J., Loizeau, J.-Luc., Pardos, M., and Arpagaus, P., 1999, Origin and
889 Evolution of Pb in Sediments of Lake Geneva (Switzerland−France). Establishing a
890 Stable Pb Record: Environmental Science & Technology, v. 33, p. 2850–2857,
891 doi:10.1021/es9902468.

892 Musial, G., Reynaud, J.-Y., Gingras, M.K., Féniès, H., Labourdette, R., and Parize, O., 2012,
893 Subsurface and outcrop characterization of large tidally influenced point bars of the
894 Cretaceous McMurray Formation (Alberta, Canada): Sedimentary Geology, v. 279, p.
895 156–172, doi:10.1016/j.sedgeo.2011.04.020.

Pace, A., Bourillot, R., Bouton, A., Vennin, E., Braissant, O., Dupraz, C., Duteil, T., Bundeleva, I., Patrier, P., Galaup, S., Yokoyama, Y., Franceschi, M., Virgone, A., and Visscher, P.T., 2018, Formation of stromatolite lamina at the interface of oxygenic-anoxygenic photosynthesis: Geobiology, v. 16, p. 378–398, doi:10.1111/gbi.12281.

Parra, M., Trouky, H., Jouanneau, J.-M., Grousset, F., Latouche, C., and Castaing, P., 1998, Étude isotopique (Sr-Nd) de l'origine des dépôts fins holocènes du littoral atlantique (S-O France): Oceanologica Acta, v. 21, p. 631–644, doi:10.1016/S0399-1784(99)80022-X.

Petschick, R., 2002, MacDiff 4.2.6 - Manual: 61 p., http://www.geol-pal.uni-frankfurt.de/Staff/Homepages/Petschick/PDFs/MacDiff%20Manual%20E.pdf.

Pittman, E.D., and Lumsden, D.N., 1968, Relationship between chlorite coatings on quartz grains and porosity, Spiro Sand, Oklahoma: Journal of Sedimentary Petrology, v. 38, p. 668–670, doi:10.1306/74D71A28-2B21-11D7-8648000102C1865D.

Pourchet, M., Pinglot, J.F., and Mélières, M.A., 1989, Cesium 137 and lead 210 in alpine lake sediments: Measurements and modeling of mixing processes: Journal of Geophysical Research, v. 94, p. 12761–12770, doi:10.1029/JC094iC09p12761.

Pranter, M.J., Ellison, A.I., Cole, R.D., and Patterson, P.E., 2007, Analysis and modeling of intermediate-scale reservoir heterogeneity based on a fluvial point-bar outcrop analog, Williams Fork Formation, Piceance Basin, Colorado: American Association of Petroleum Geologists, Bulletin, v. 91, p. 1025–1051, doi:10.1306/02010706102.

Roduit, N., 2007, JMicroVision: un logiciel d'analyse d'images pétrographiques polyvalent: Section de Sciences de la Terre, Université de Genève, 116 p., 10.13097/archive-ouverte/unige:468.

Saïag, J., Brigaud, B., Portier, É., Desaubliaux, G., Bucherie, A., Miska, S., and Pagel, M., 2016, Sedimentological control on the diagenesis and reservoir quality of tidal sandstones of the Upper Cape Hay Formation (Permian, Bonaparte Basin, Australia): Marine and Petroleum Geology, v. 77, p. 597–624, doi:10.1016/j.marpetgeo.2016.07.002.

Sarkar, S., Banerjee, S., Eriksson, P.G., and Catuneanu, O., 2005, Microbial mat control on siliciclastic Precambrian sequence stratigraphic architecture: Examples from India: Sedimentary Geology, v. 176, p. 195–209, doi:10.1016/j.sedgeo.2004.12.012.

Shchepetkina, A., Gingras, M.K., and Pemberton, S.G., 2018, Modern observations of floccule ripples: Petitcodiac River estuary, New Brunswick, Canada: Sedimentology, v. 65, p. 582–596, doi:10.1111/sed.12393.

Shchepetkina, A., Gingras, M.K., and Pemberton, S.G., 2016a, Sedimentology and ichnology of the fluvial reach to inner estuary of the Ogeechee River estuary, Georgia, USA: Sedimentary Geology, v. 342, p. 202–217, doi:10.1016/j.sedgeo.2016.07.005.

Shchepetkina, A., Gingras, M.K., Zonneveld, J.-P., and Pemberton, S.G., 2016b, Sedimentary fabrics of the macrotidal, mud-dominated, inner estuary to fluvio-tidal transition zone, Petitcodiac River estuary, New Brunswick, Canada: Sedimentary Geology, v. 333, p. 147–163, doi:10.1016/j.sedgeo.2015.12.015.

Shchepetkina, A., Gingras, M.K., Zonneveld, J.-P., and Pemberton, S.G., 2017, Silt- and Bioclastic-Rich Flocs and Their Relationship to Sedimentary Structures: Modern Observations from the Petitcodiac River Estuary: Estuaries and Coasts, v. 40, p. 947–966, doi:10.1007/s12237-016-0186-x.

Smith, D.J., and Underwood, G.J.C., 1998, Exopolymer production by intertidal epipelic diatoms: Limnology and Oceanography, v. 43, p. 1578–1591, doi:10.4319/lo.1998.43.7.1578.

Sottolichio, A., Castaing, P., Etcheber, H., Maneux, E., Schmeltz, M., and Schmidt, S., 2011, Observations of suspended sediment dynamics in a highly turbid macrotidal estuary, derived from continuous monitoring: Journal of Coastal Research, v. 64, p. 1579–1583.

Stoodley, P., Cargo, R., Rupp, C.J., Wilson, S., and Klapper, I., 2002, Biofilm material properties as related to shear-induced deformation and detachment phenomena: Journal of Industrial Microbiology and Biotechnology, v. 29, p. 361–367, doi:10.1038/sj.jim.7000282.

Stricker, S., Jones, S.J., Sathar, S., Bowen, L., and Oxtoby, N., 2016, Exceptional reservoir quality in HPHT reservoir settings: Examples from the Skagerrak Formation of the Heron Cluster, North Sea, UK: Marine and Petroleum Geology, v. 77, p. 198–215, doi:10.1016/j.marpetgeo.2016.02.003.

Sun, Z.-X., Sun, Z.-L., Yao, J., Wu, M.-L., Liu, J.-R., Dou, Z., and Pei, C., 2014, Porosity preservation due to authigenic chlorite coatings in deeply buried Upper Triassic Xujiahe Formation Sandstones, Sichuan Basin, Western China: Journal of Petroleum Geology, v. 37, p. 251–267, doi:10.1111/jpg.12582.

Taylor, T.R., Giles, M.R., Hathon, L.A., Diggs, T.N., Braunsdorf, N.R., Birbiglia, G.V., Kittridge, M.G., Macaulay, C.I., and Espejo, I.S., 2010, Sandstone diagenesis and reservoir quality prediction: Models, myths, and reality: American Association of Petroleum Geologists, Bulletin, v. 94, p. 1093–1132, doi:10.1306/04211009123.

Thomson, A., 1979, Preservation of porosity in the deep Woodbine/Tuscaloosa Trend, Louisiana, *in* Gulf Coast Association of Geological Societies Transactions, San Antonio, Texas, 29th Annual Meeting, v. 29, p. 396–403.

Underwood, G.C., and Kromkamp, J., 1999, Primary production by phytoplankton and microphytobenthos in estuaries: Advances in ecological research, v. 29, p. 93–153.

Verhagen, I.T.E., Crisóstomo-Figueroa, A., Utley, J.E.P., and Worden, R.H., 2020, Abrasion of detrital grain-coating clays during sediment transport: Implications for diagenetic clay coats: Sedimentary Geology, p. 105653, doi:10.1016/j.sedgeo.2020.105653.

Virolle, M., Brigaud, B., Bourillot, R., Féniès, H., Portier, E., Duteil, T., Nouet, J., Patrier, P., and Beaufort, D., 2019a, Detrital clay grain coats in estuarine clastic deposits: origin and spatial distribution within a modern sedimentary system, the Gironde Estuary (south-west France): Sedimentology, v. 66, p. 859–894, doi:10.1111/sed.12520.

Virolle, M., Brigaud, B., Luby, S., Portier, E., Féniès, H., Bourillot, R., Patrier, P., and Beaufort, D., 2019b, Influence of sedimentation and detrital clay grain coats on

chloritized sandstone reservoir qualities: Insights from comparisons between ancient tidal heterolithic sandstones and a modern estuarine system: Marine and Petroleum Geology, v. 107, p. 163–184, doi:10.1016/j.marpetgeo.2019.05.010.

Virolle, M., Féniès, H., Brigaud, B., Bourillot, R., Portier, E., Patrier, P., Beaufort, D., Jalon-Rojas, I., Derriennic, H., and Miska, S., 2020, Facies associations, detrital clay grain coats and mineralogical characterization of the Gironde estuary tidal bars: A modern analogue for deeply buried estuarine sandstone reservoirs: Marine and Petroleum Geology, p. 104225, doi:https://doi.org/10.1016/j.marpetgeo.2020.104225.

Visser, M.J., 1980, Neap-spring cycles reflected in Holocene subtidal large-scale bedform deposits: a preliminary note: Geology, v. 8, p. 543–546.

Webb, R.H., O'Connor, J.E., and Baker, V., 1988, Paleohydrologic reconstruction of flood frequency on the Escalante River, south-central Utah, *in* Baker, V., Kochel, R.C., and Patton, P.C. eds., Flood Geomorphology, Wiley-Interscience, p. 403–418.

Williams, H.F.L., and Hamilton, T.S., 1995, Sedimentary Dynamics of an Eroding Tidal Marsh Derived from Stratigraphic Records of ^{137}Cs Fallout, Fraser Delta, British Columbia, Canada: Journal of Coastal Research, v. 11, p. 1145–1156.

Wooldridge, L.J., Worden, R.H., Griffiths, J., Thompson, A., and Chung, P., 2017a, Biofilm origin of clay-coated sand grains: Geology, v. 45, p. 875–878, doi:10.1130/G39161.1.

Wooldridge, L.J., Worden, R.H., Griffiths, J., and Utley, J.E.P., 2019a, Clay- coat diversity in marginal marine sediments: Sedimentology, doi:10.1111/sed.12538.

Wooldridge, L.J., Worden, R.H., Griffiths, J., and Utley, J.E.P., 2017b, Clay-Coated Sand Grains in Petroleum Reservoirs: Understanding Their Distribution Via a Modern Analogue: Journal of Sedimentary Research, v. 87, p. 338–352, doi:10.2110/jsr.2017.20.

Wooldridge, L.J., Worden, R.H., Griffiths, J., and Utley, J.E.P., 2019b, How to Quantify Clay-Coat Grain Coverage in Modern and Ancient Sediments: Journal of Sedimentary Research, v. 89, p. 135–146, doi:10.2110/jsr.2019.6.

Worden, R.H., Griffiths, J., Wooldridge, L.J., Utley, J.E.P., Lawan, A.Y., Muhammed, D.D., Simon, N., and Armitage, P.J., 2020, Chlorite in sandstones: Earth-Science Reviews, v. 204, p. 103105, doi:10.1016/j.earscirev.2020.103105.

Worden, R.H., and Morad, S., 2003, Clay Minerals in Sandstones: Controls on Formation, Distribution and Evolution, *in* Worden, R.H. and Morad, S. eds., Clay Mineral Cements in Sandstones, Oxford, UK, Blackwell Publishing Ltd., p. 3–41, doi:10.1002/9781444304336.ch1.

Figure 1

Click here to access/download;Figure;Figure1_2019-PB contexte-V3.jpg

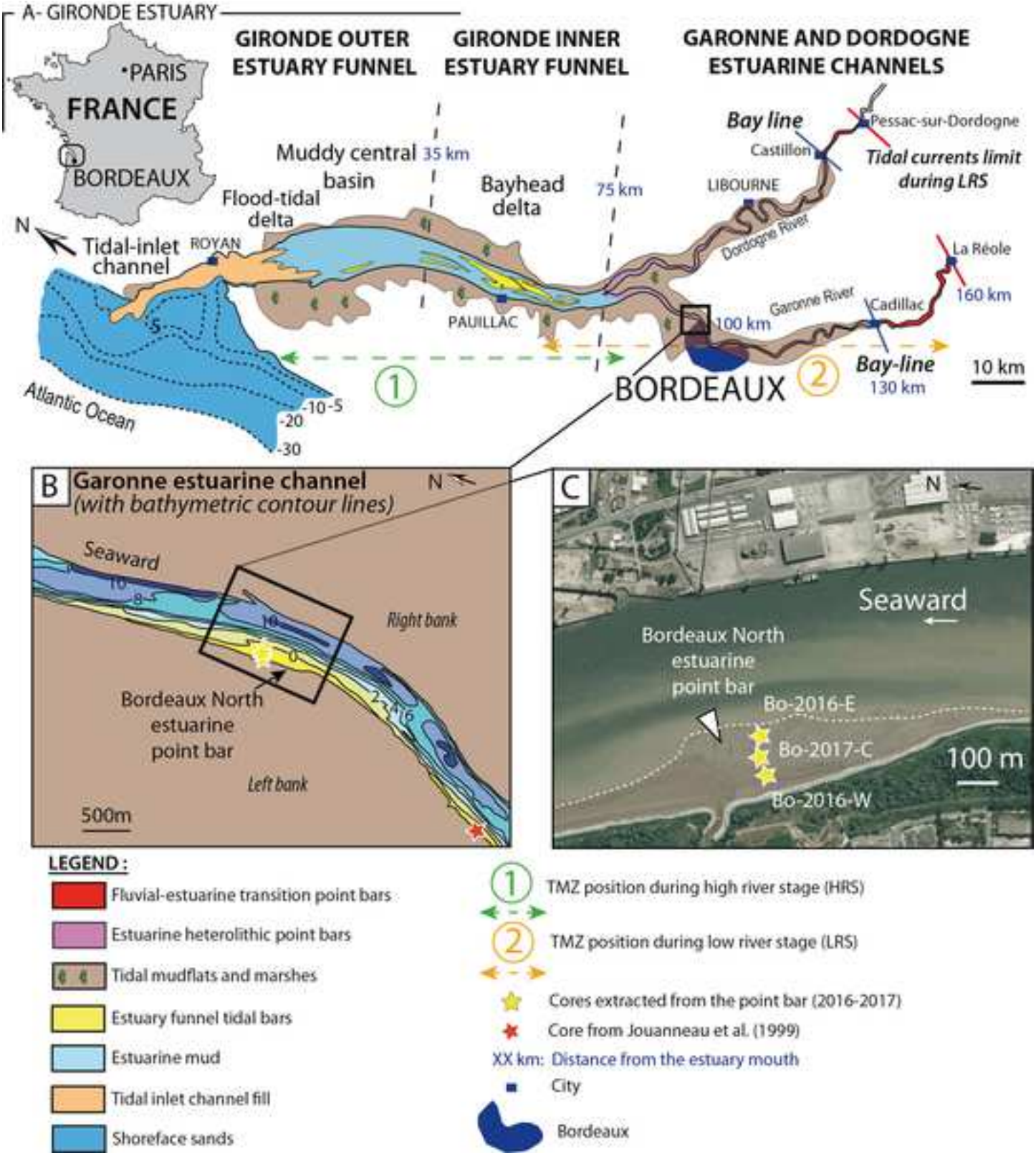

Figure 2

Click here to access/download;Figure;Figure2_2019-03-log-synthetique-Bordeaux-facies-V5-2.jpg

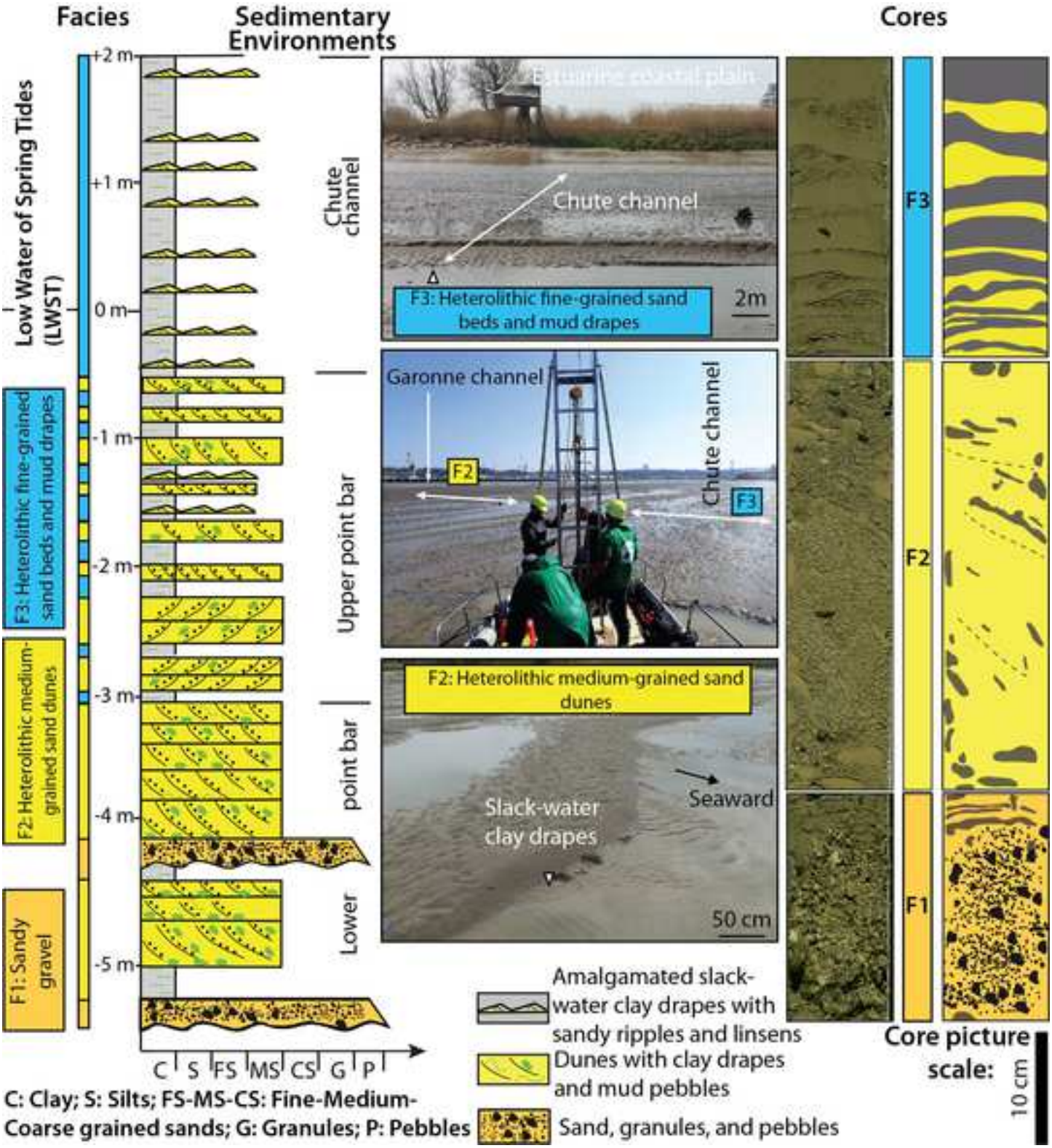

Figure 3

Click here to access/download;Figure;Figure3_2019-QFL papier point bar.jpg

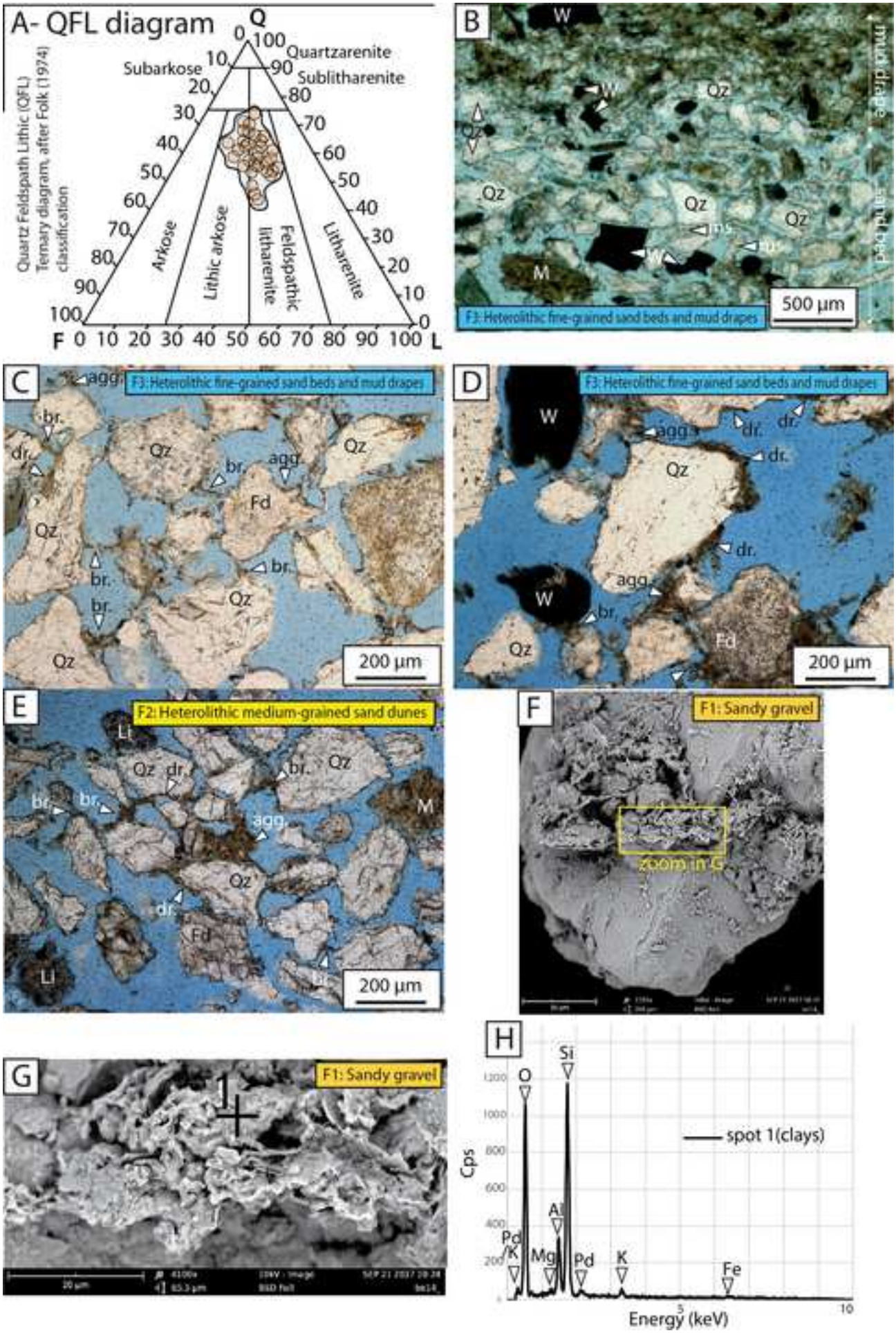

Figure 4

Click here to access/download;Figure;Figure4_2019-03-Transect-BdxN-Facies V6.eps

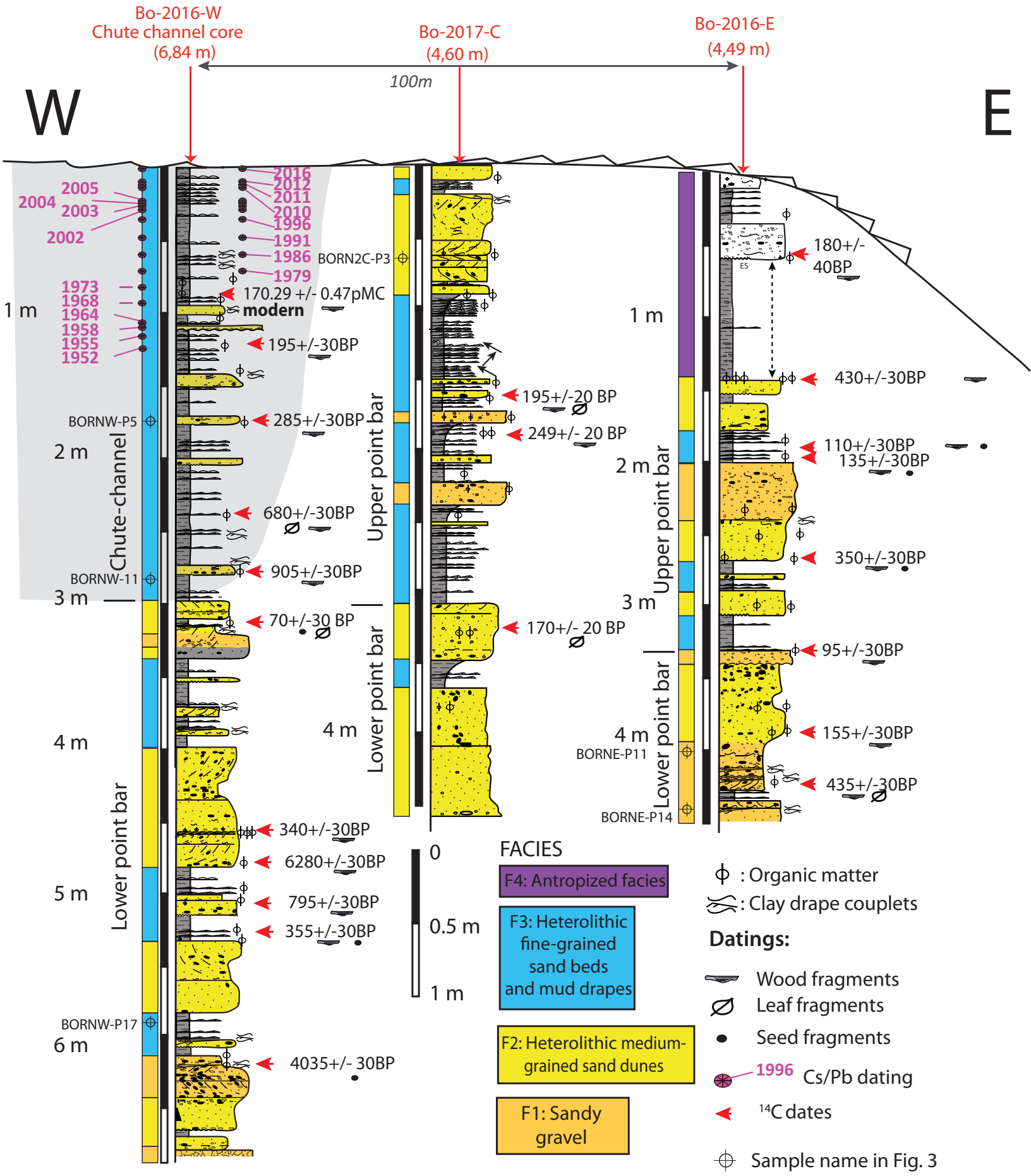

Figure 5

Click here to access/download;Figure;Figure5_2018-Fig datations Cs Pb-V3.jpg

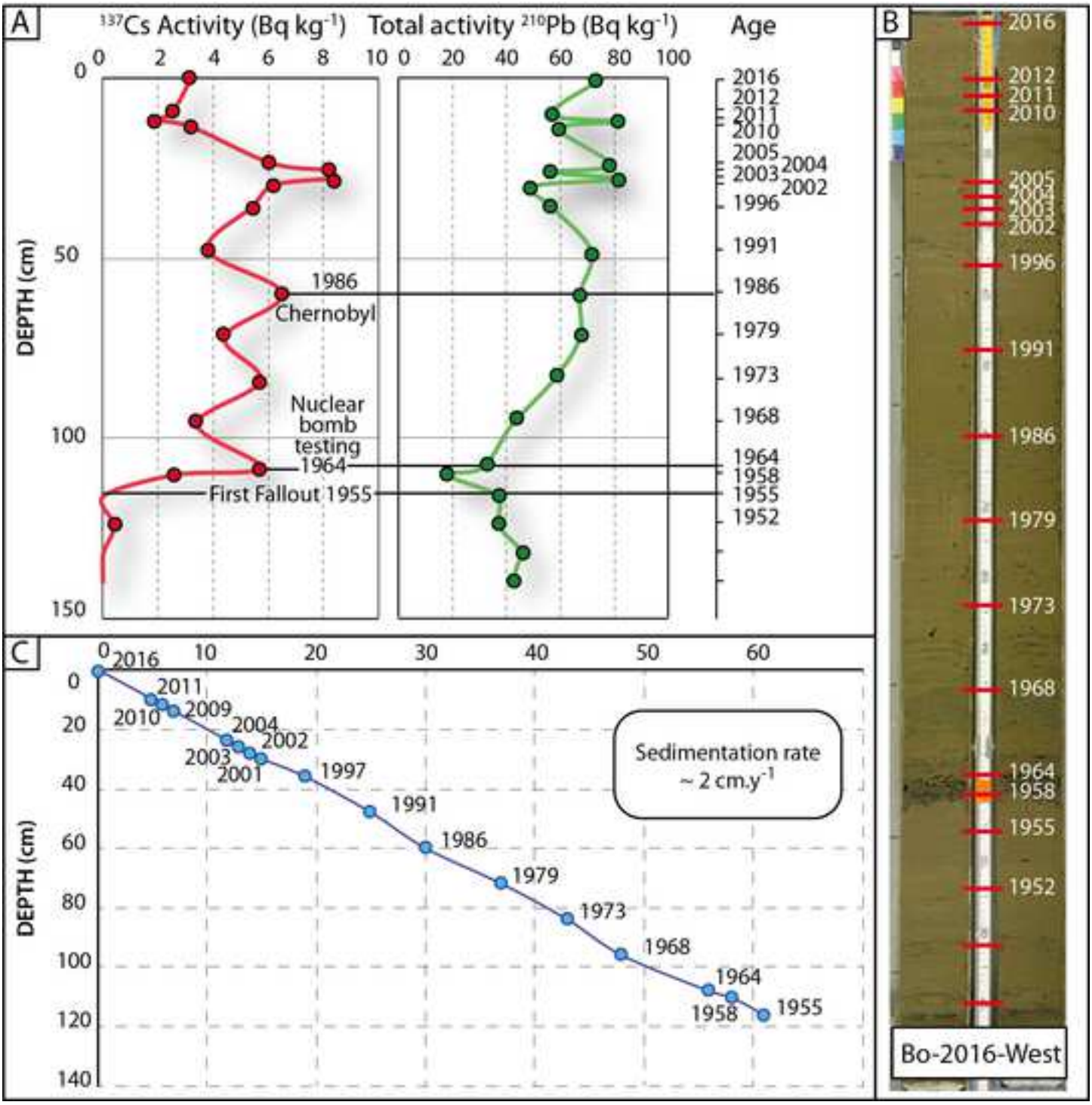

Figure 6

Click here to access/download;Figure;Figure6_Diatoms point bar.jpg

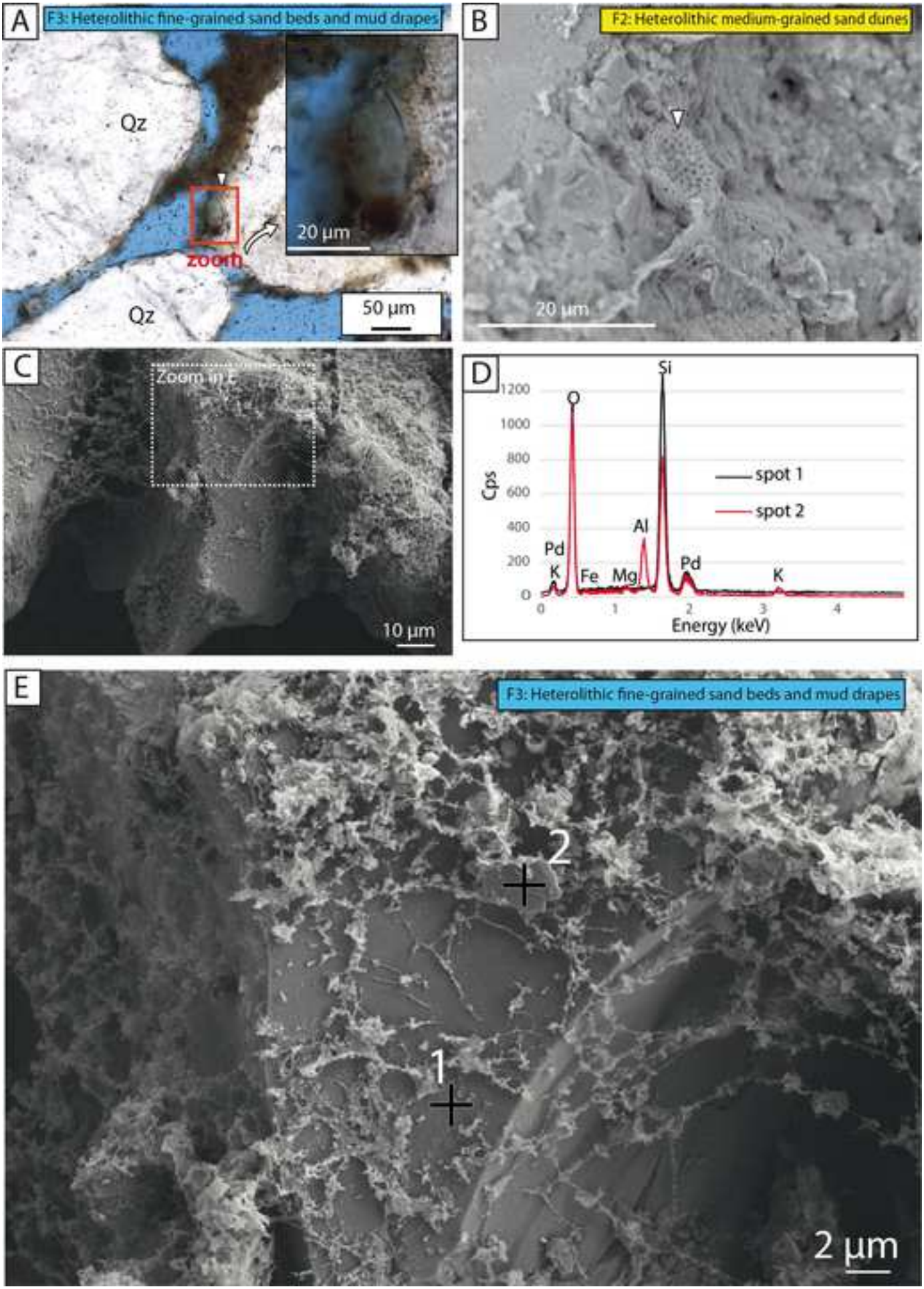

Figure 7

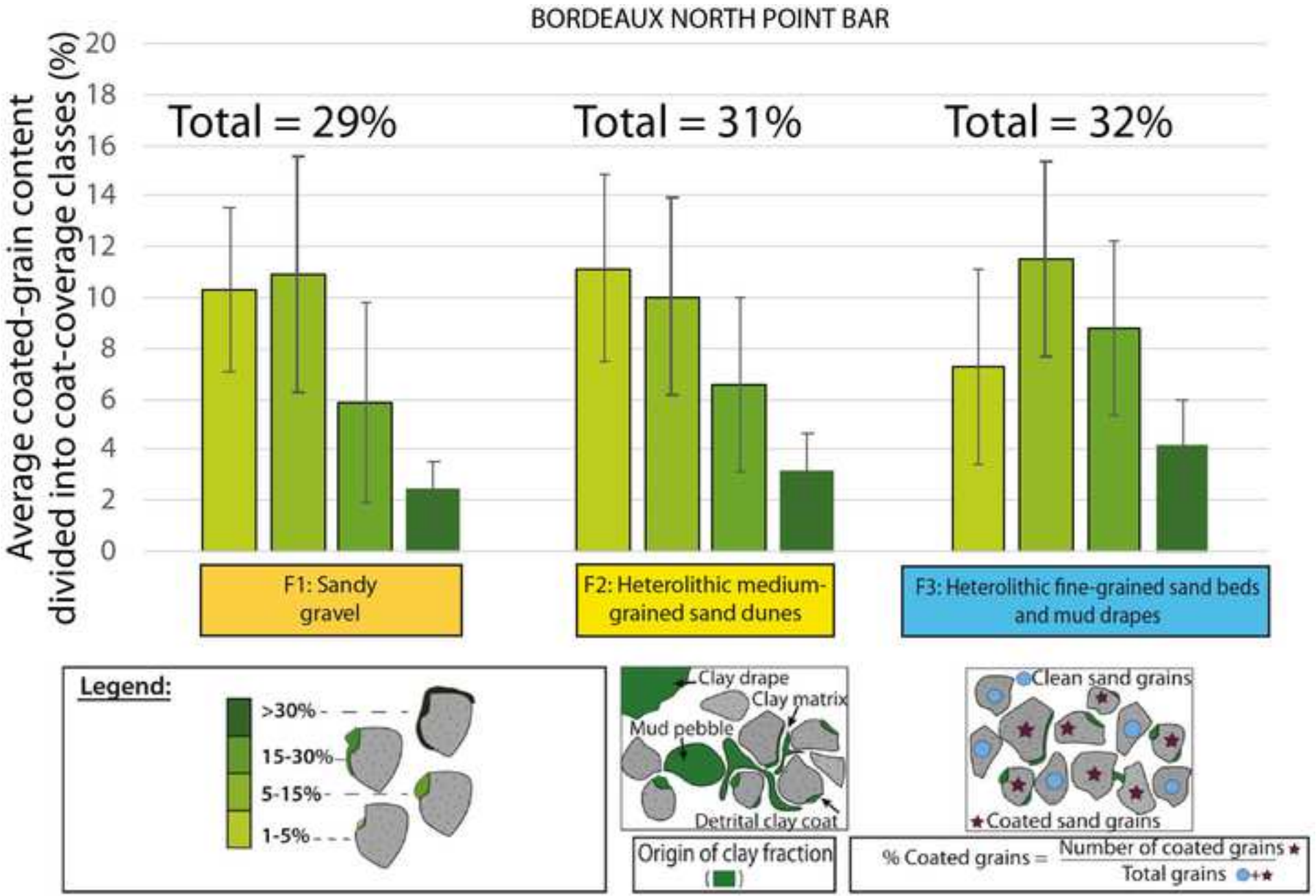

Figure 8

Click here to access/download;Figure;Figure8_2019-Bordeaux planche article-V5.eps

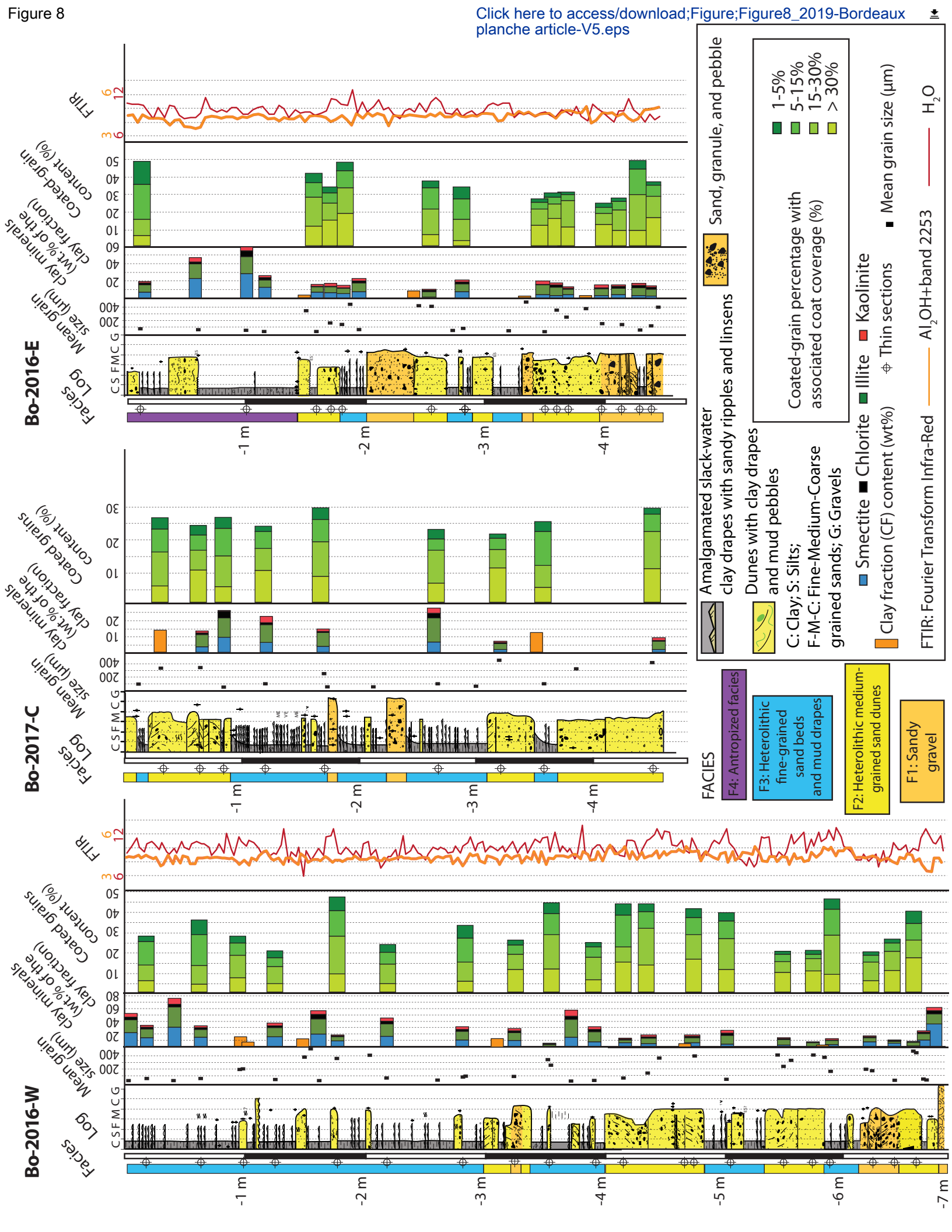

Figure 9

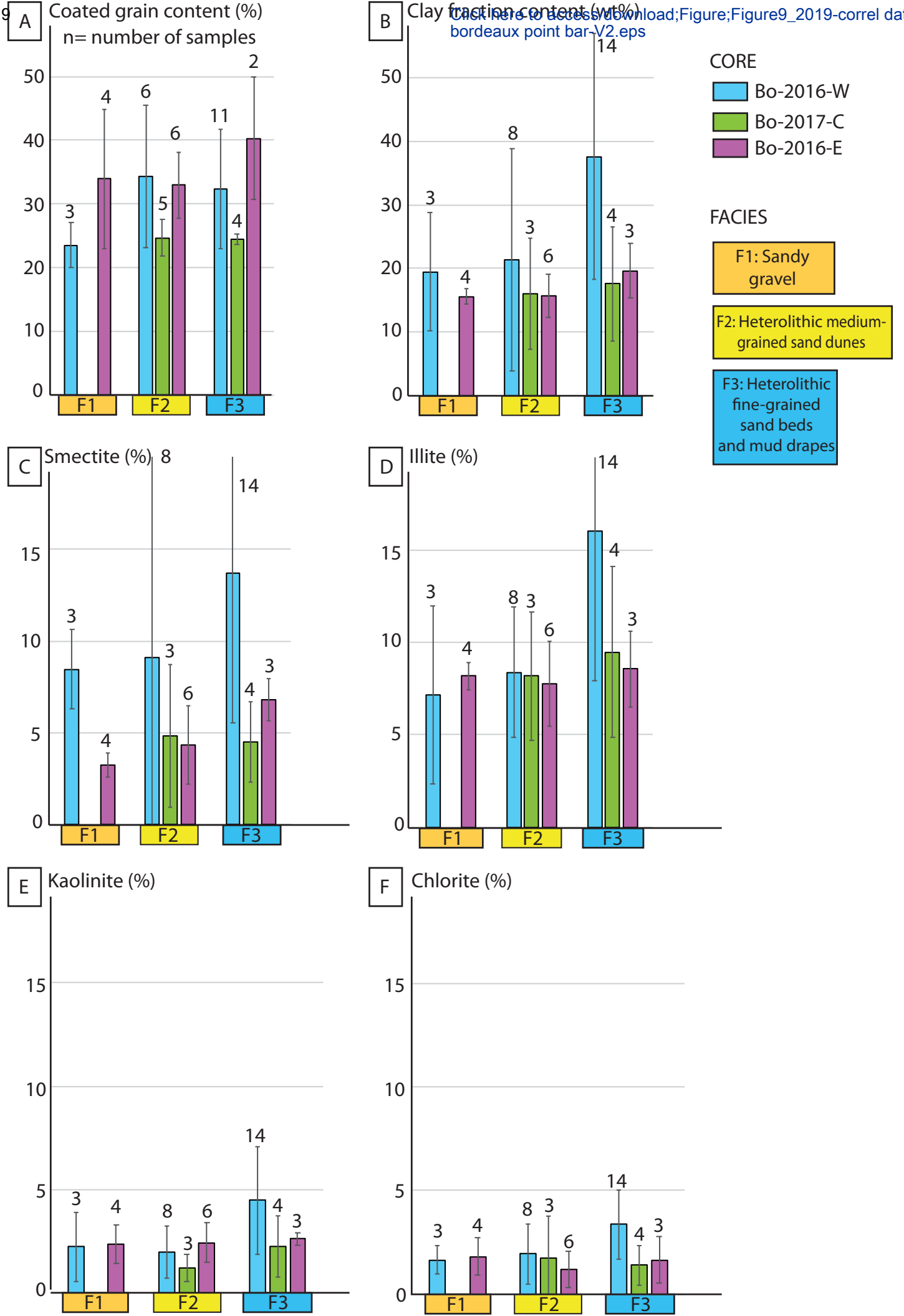

Figure 10

Click here to access/download;Figure;Figure10_XRD point bar bordeaux.eps

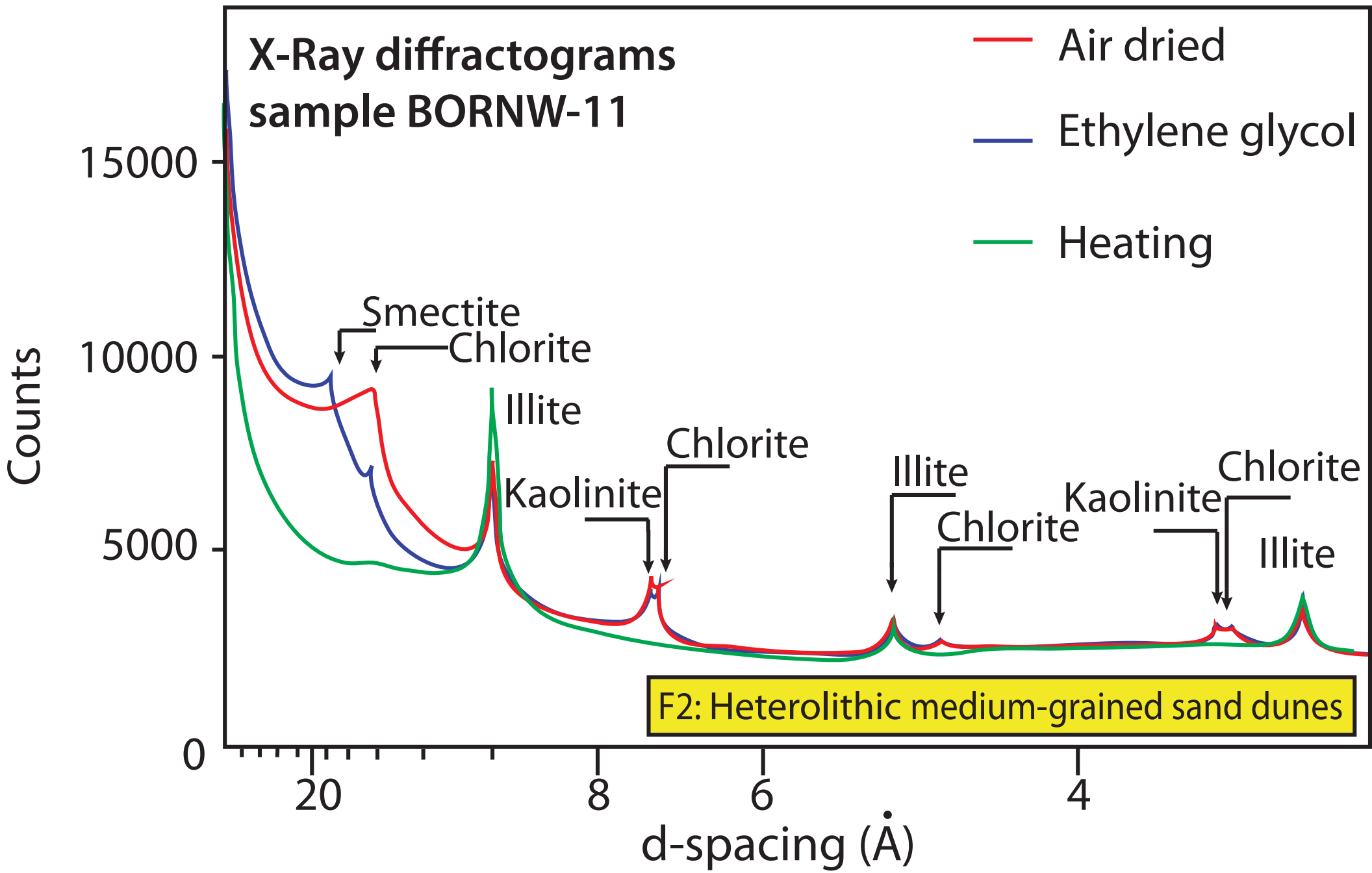

Figure 11

Click here to access/download;Figure;Figure11_2019-PG migration through time-V2.jpg

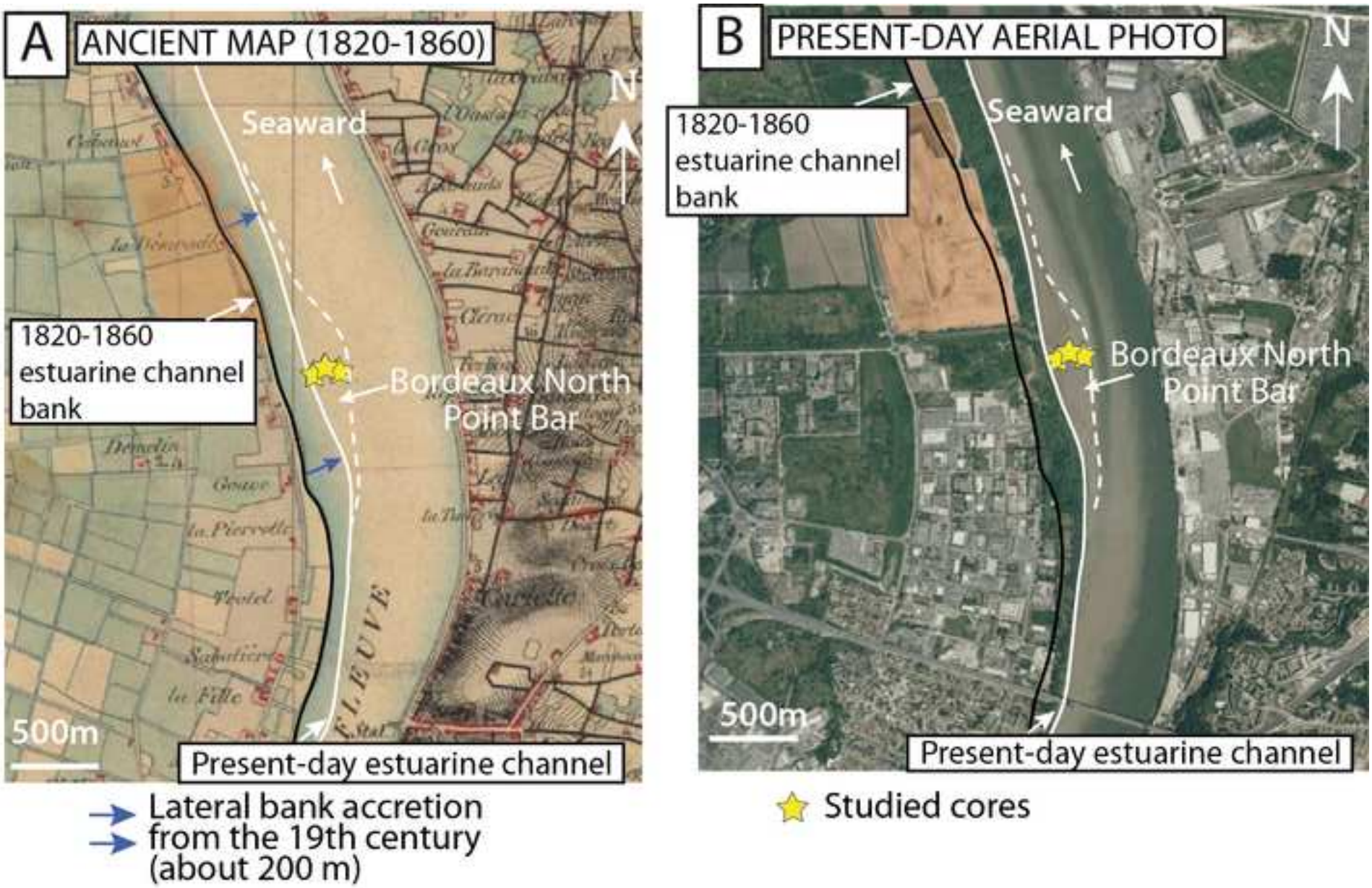

Figure 12

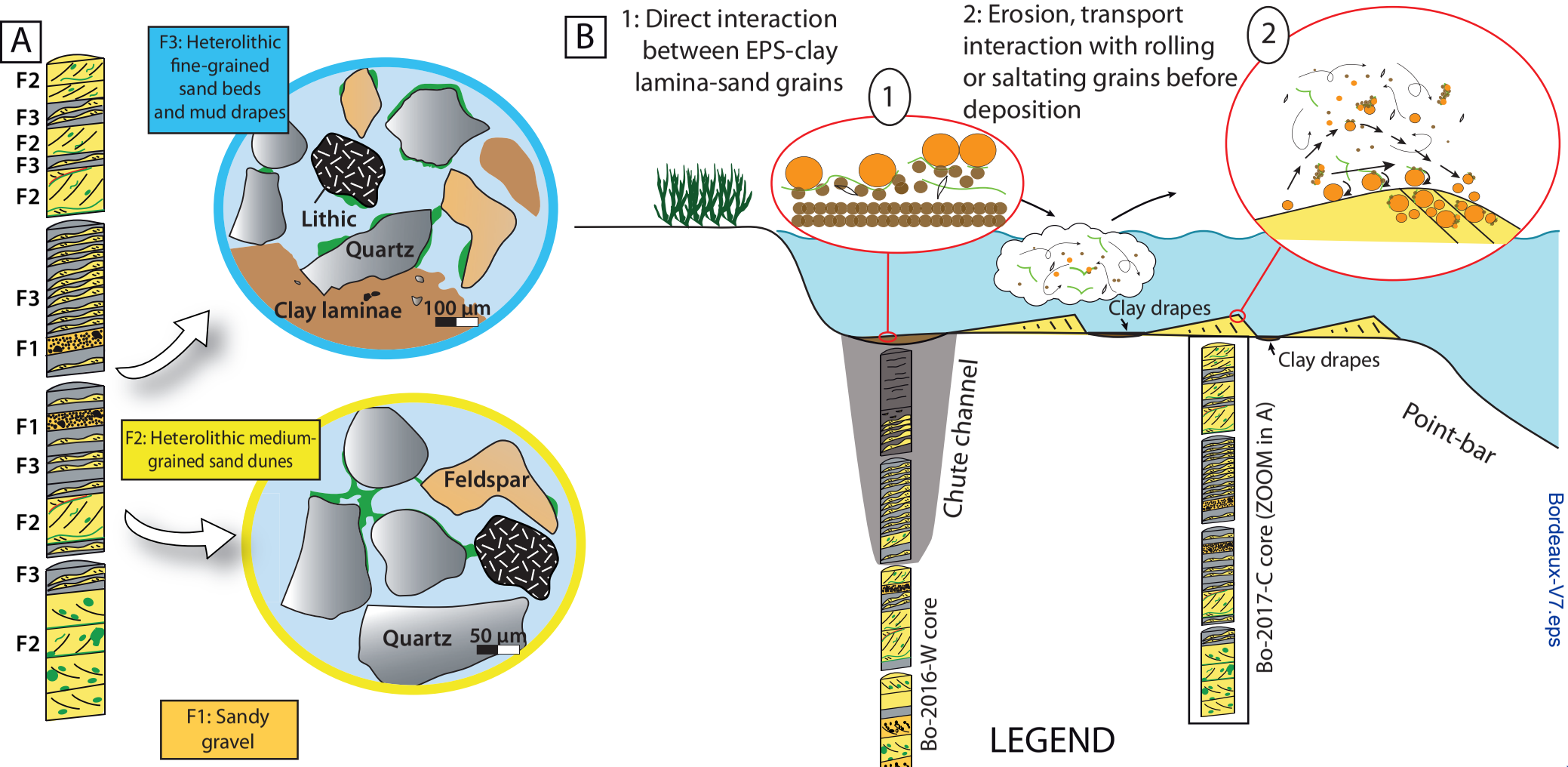

C

Facies	Smectite	Illite	Chlorite	Kaolinite	Clay fraction content (wt%)	Coated-grain content (%)
F1	6	8	2	2	18	29
F2	6	8	2	2	18	31
F3	8	11	2	3	25	32
Total	7	9	2	2	20	32

Facies number	Facies name	Facies description	Texture	Thickness	Set thickness	Location in the bar
F1	Sandy gravel	Coarse-grained sands, pebbles, gravels with no sedimentary structures. It contains shells and shell fragments and mud clasts, wood, seed, or leaf debris.	Mean grain size: 209 µm. Grains are mostly subrounded and poorly sorted	At least centimeter thick, decimeter thick	/	Lower part
F2	Heterolithic medium-grained sand dunes	Sands with 5–30% clayey interbeds Small- to medium-size sand-rich dunes with few coarse mud pebbles on foresets and bottomsets or with thin clay drapes on foresets and bottomsets. Mud pebbles subrounded to subangular. Bottomsets are sometimes composed of thick individual horizontal clay drapes or thick amalgamated clay drapes. Some counter reactivation surfaces and clay drapes couplets are preserved. No bioturbation	Mean grain size: 266 µm. Grains are subrounded to subangular and moderately well sorted to poorly sorted	Decimeter to meter thick	Mean thickness of 12 cm	Lower part
F3	Heterolithic fine-grained sand beds and mud drapes	Clays with 10–30% sand interbeds Centimeter-to-decimeter-thick mud layers or centimetre-thick clay drapes alternating with sandy ripples, sandy to silty linsens, and rare small sand dunes with clay drapes on foresets and bottomsets. Mud layers may sometimes correspond to stacked amalgamated clay drapes. Neap-spring cycle may be recorded in this facies with millimetric alternations of thinly-bedded fine-grained silty linsen to centimeter-thick ripples with amalgamated clay drapes. Rare bioturbation observed (*Planolites* sp.?)	Mean grain size: 138 µm. Grains are subrounded to subangular and moderately well sorted	Decimeter to meter thick		Upper part
F4	Admixed and anthropized sand and mud facies	Mud-dominated facies composed of a mix of highly disturbed and anthropized sand and mud with many elements left by humans such as pieces of brick or shipyard bolts. Coarse-grained sand sometimes mixed within mud	Mean grain size: 69 µm	Meter thick	/	

Table 1

Facies	Grain composition - JmicroVision Image analysis on thin sections							Coated-grain content and coat coverage classes (percentage of the outer surface coated) - JmicroVision Image analysis on thin sections					Clay-fraction content - relative weight percentage of the clay fraction of homogenized sediment	Compositions of the clay fraction (< 2 µm) - X-ray diffraction (XRD)			
	Quartz (%)	Feldspars (%)	Lithic grains (%)	Carbonates (%)	Clays (%)	Macroporosity (%)	Micas (%)	1-5%	5-15%	15-30%	> 30%	Total coated grains (%)	Clay-fraction content (wt%)	% Smectite	% Illite	% Chlorite	% Kaolinite
F1	38	10	14	5	15	13	5	10	11	6	2	29	18	6	8	2	2
F2	39	12	14	2	13	14	5	11	10	7	3	31	18	6	8	2	2
F3	34	10	14	3	23	13	5	7	12	9	4	32	25	8	11	2	3
Total/Mean	37	11	14	3	17	13	5	10	11	7	3	31	20	7	9	2	2

Table 2

Table 3

Depth		^{210}Pb						^{137}Cs	
		Total		Unsupported		Supported			
cm	g cm^{-2}	Bq kg^{-1}	±	Bq kg^{-1}	±	Bq kg^{-1}	±	Bq kg^{-1}	±
0.5	0.5	74.2	6	38.2	6.2	36	1.4	3.2	0.7
10	9.8	56.8	3.8	18	3.9	38.8	0.9	2.5	0.5
12	12.2	81.3	5.6	5.8	5.8	75.5	1.5	1.9	0.7
14	14.3	59.7	3.5	17.2	3.6	42.5	0.8	3.2	0.4
24	25.3	78.3	6.3	25.6	6.5	52.7	1.5	6.1	0.8
26	27.1	56.6	4.8	12	4.9	44.6	1.2	8.2	0.8
28	28.8	81.7	7	32.5	7.2	49.2	1.6	8.4	0.9
30	30.6	49.7	5.5	10.6	5.6	39.1	1.3	6.2	0.7
36	37.8	57.3	5.6	11.8	5.8	45.5	1.3	5.4	0.9
48	50	71.4	6.9	22.8	7.1	48.6	1.7	3.8	0.8
60	60.8	67.2	6.8	22.9	7	44.3	1.7	6.5	1.1
72	74.9	67.2	5.9	22.5	6	44.7	1.4	4.4	0.8
84	86.6	57.1	5.8	8.7	6	48.4	1.5	5.7	0.9
96	98.6	42.1	4.5	5.3	4.6	36.7	1.1	3.4	0.7
108	114	31.2	3.8	-0.7	3.9	31.9	0.9	5.7	0.6
110	117.2	17.9	2.3	1.5	2.4	16.3	0.6	2.6	0.4
116	123.3	36.9	4.2	0.4	4.3	36.5	1.1	0	0
124	131.3	37	5.1	-2.2	5.3	39.3	1.3	0.4	0.8
132	141.3	45.8	4.2	8	4.3	37.8	1	0	0
140	150.8	42.7	3.9	5.5	4	37.2	0.9	0	0
234	277.6	42.9	4.1	3.9	4.2	39	1	0.4	0.5

Appendix 1

Click here to access/download;Appendices;Appendix 1.xlsx

CLAY MINERALOGY X-RAY DIFFRACTOMMETER

Sample		Facies	% Clay	% Smectite	% Illite
CORE Bo-2016-West					
Bdx-West-GR-1	100 cm	F3			
Bdx-West-GR-2	148 cm	F3			
Bdx-West-GR-3	205 cm	F3			
Bdx-West-GR-4	283 cm	F3			
Bdx-West-GR-5	310 cm	F2			
Bdx-West-GR-6	357 cm	F3			
Bdx-West-GR-7	445 cm	F2			
Bdx-West-GR-8	475 cm	F2			
Bdx-West-GR-9	545 cm	F2			
Bdx-West-GR-10	585 cm	F2			
Bdx-West-GR-11	623 cm	F1			
Bdx-West-GR-12	660 cm	F2			
BORNW-01	2 cm	F3	53	23	20
BORNW-02	18 cm	F3	34	15	14
BORNW-03	41 cm	F3	77	32	32
BORNW-04	63 cm	F3	34	15	12
BORNW-05	97 cm	F3			
BORNW-06	127 cm	F3	38	16	15
BORNW-07	161 cm	F3	57	21	24
BORNW-08	179 cm	F3	19	10	7
BORNW-09	218 cm	F3	46	17	20
BORNW-10	260 cm	F3			
BORNW-11	281 cm	F3	32	11	14
BORNW-12	323 cm	F1	29	11	12
BORNW-13	359 cm	F3	6	1	3
BORNW-14	371 cm	F3	58	15	28
BORNW-15	390 cm	F3	32	8	16
BORNW-16	415 cm	F2	14	7	5
BORNW-17	435 cm	F2	19	5	9
BORNW-18	471 cm	F2	19	6	8
BORNW-19	504 cm	F3	26	5	14
BORNW-20	550 cm	F2	15	3	8
BORNW-21	575 cm	F2	8	1	5
BORNW-22	590 cm	F3	13	4	7
BORNW-23	625 cm	F1	18	9	6
BORNW-24	645 cm	F1	11	6	3
BORNW-25	661 cm	F2	9	2	6
BORNW-26	666 cm	F2	25	11	10
BORNW-27	675 cm	F2	62	37	16
CORE Bo-2017-Center					
BORN2C-GR-1	31 cm	F2			
BORN2C-GR-2	64 cm	F2			
BORN2C-GR-3	170 cm	F3			

BORN2C-GR-4	320 cm	F2			
BORN2C-GR-5	385 cm	F2			
BORN2C-GR-6	450 cm	F2			
BORNC-01	11 cm	F3			
BORN2C-02	84 cm	F2	13	4	7
BORN2C-03	90 cm	F2	26	9	12
BORN2C-04	120 cm	F3	22	6	11
BORN2C-05	170 cm	F3	14	4	8
BORN2C-06	267 cm	F3	27	6	15
BORN2C-07	320 cm	F3	7	2	4
BORN2C-08	450 cm	F2	9	2	5
CORE Bo-2016-East					
Bdx-est-GR-1	150 cm	F2			
Bdx-est-GR-2	185 cm	F3			
Bdx-est-GR-3	245 cm	F1			
Bdx-est-GR-4	335 cm	F1			
Bdx-est-GR-5	385 cm	F2			
Bdx-est-GR-6	444 cm	F1			
BORNE-01	11 cm	F4	20	7	8
BORNE-02	58 cm	F4	47	23	17
BORNE-03	100 cm	F4	60	28	20
BORNE-04	115 cm	F4	26	13	8
BORNE-05	160 cm	F2	16	7	6
BORNE-06	170 cm	F2	17	7	7
BORNE-07	180 cm	F3	15	5	6
BORNE-08	195 cm	F3	23	8	10
BORNE-09	255 cm	F2	10	1	6
BORNE-10	273 cm	F3			
BORNE-11	281 cm	F3	21	7	9
BORNE-12	320 cm	F3			
BORNE-13	350 cm	F2	20	4	11
BORNE-14	360 cm	F2	18	3	10
BORNE-15	368 cm	F2	13	4	6
BORNE-16	400 cm	F1	16	3	8
BORNE-17	415 cm	F1	15	4	8
BORNE-18	430 cm	F1	17	3	9
BORNE-19	438 cm	F1	14	3	8

IMAGE ANALYSIS ON THIN SECTION					
			Quartz	**Felsdpars**	**Lithic**
CORE Bo-2016-West					
BORNW1-P-1	18 cm	F3	26	12	10
BORNW1-P-2	63 cm	F3	30	11	14
BORNW1-P-3	97 cm	F3	34	12	19
BORNW1-P-4	127 cm	F3	21	11	14
BORNW1-P-5	179 cm	F3	40	11	15

BORNW1-P-6	218 cm	F3	25	7	10
BORNW1-P-7	281 cm	F3	32	8	11
BORNW1-P-8	323 cm	F1	33	9	10
BORNW1-P-9	359 cm	F3	37	11	21
BORNW1-P-10	390 cm	F3	29	9	14
BORNW1-P-11	415 cm	F2	33	15	19
BORNW1-P-12	435 cm	F2	33	17	21
BORNW1-P-13	471 cm	F2	42	15	8
BORNW1-P-14	504 cm	F3	41	8	10
BORNW1-P-15	550 cm	F2	46	9	15
BORNW1-P-16	575 cm	F2	43	13	12
BORNW1-P-17	590 cm	F3	40	15	12
BORNW1-P-18	625 cm	F1	42	9	8
BORNW1-P-19	645 cm	F1	40	9	24
BORNW1-P-20	661 cm	F2	48	11	11
CORE Bo-2017-Center					
BORN2C-P1	31 cm	F2	37	13	15
BORN2C-P2	64 cm	F2	42	10	15
BORN2C-P3	84 cm	F2	34	10	10
BORN2C-P4	120 cm	F3	29	9	15
BORN2C-P5	170 cm	F3	40	12	13
BORN2C-P6	267 cm	F3	34	9	10
BORN2C-P7	320 cm	F2	44	16	13
BORN2C-P8	358 cm	F3	36	7	14
BORN2C-P9	450 cm	F2	41	17	13
CORE Bo-2016-East					
BORNE1-P-1	100 cm	F4	41	11	12
BORNE1-P-3	160 cm	F2	35	13	17
BORNE1-P-4	170 cm	F2	39	7	14
BORNE1-P-5	180 cm	F3	49	7	12
BORNE1-P-6	255 cm	F2	42	10	11
BORNE1-P-7	281 cm	F3	36	8	18
BORNE1-P-8	350 cm	F2	32	10	14
BORNE1-P-9	360 cm	F2	35	7	16
BORNE1-P-10	368 cm	F2	42	12	12
BORNE1-P-11	400 cm	F1	35	10	9
BORNE1-P-12	415 cm	F1	45	9	10
BORNE1-P-13	430 cm	F1	38	14	17
BORNE1-P-14	438 cm	F1	35	11	20

% Chlorite	% Kaolinite	mean grain size
		201
		394
		411
		98
		349
		325
		370
		397
		408
		383
		192
		461
4	6	38
3	3	74
4	9	36
3	3	76
		199
3	4	52
7	6	35
2	1	365
4	5	74
		47
3	4	93
2	4	92
1	1	270
5	9	35
3	5	38
1	2	78
2	3	138
2	2	74
4	4	51
2	1	244
1	1	402
1	2	161
2	2	179
1	1	41
1	1	443
2	2	47
5	4	31
		334
		346
		248

		462
		342
		422
		101
1	1	56
4	1	102
1	4	71
1	1	56
3	3	105
1	1	74
0	2	91
		342
		447
		427
		492
		379
		399
2	2	89
2	5	75
7	5	61
3	2	50
1	2	43
0	3	168
0	3	126
3	3	68
2	1	414
		57
2	2	85
		51
1	4	49
3	2	360
1	2	253
1	4	159
2	2	142
3	2	56
2	2	120

						Coated grains
CaCO3	**Clays**	**Porosity**	**Others**	1-5%	5-15%	15-30%
2	32	16	3	6	8	11
2	33	7	4	4	9	15
5	14	12	5	7	11	6
4	37	10	3	4	8	4
0	17	11	5	9	18	12

2	46	7	4	4	10	6
2	31	14	3	5	9	12
2	29	13	3	11	7	4
3	6	17	5	11	17	10
4	31	6	7	6	11	5
1	9	19	4	15	7	16
0	13	12	4	13	18	8
1	18	13	3	16	12	8
3	26	8	4	11	15	9
1	10	16	2	10	5	4
2	8	16	5	10	6	2
1	12	13	7	9	19	13
3	17	14	7	5	9	3
3	8	9	7	10	9	4
3	9	11	6	17	8	8
3	12	15	5	5	10	7
3	10	15	5	10	6	5
2	25	15	4	5	9	8
4	22	17	4	10	7	5
5	14	13	4	8	10	7
1	27	16	3	6	10	3
1	7	15	4	10	6	3
4	17	16	6	4	7	10
1	8	14	6	10	11	5
2	18	13	4	6	9	20
3	15	12	4	11	16	8
2	17	14	8	15	9	6
1	15	13	4	18	15	10
4	10	19	4	6	15	12
1	10	20	7	3	12	12
4	19	15	7	12	9	4
3	14	17	7	15	8	4
6	13	9	5	11	15	4
8	15	18	5	12	6	4
5	14	12	4	9	12	5
2	14	9	5	9	20	15
8	8	13	5	16	12	6

> 30%	Total coated grain content
2	27
7	35
3	27
3	20
7	46

4	23
6	32
2	25
5	43
2	24
5	43
4	43
4	40
4	39
1	20
2	20
5	45
2	19
2	26
6	39
3	25
3	23
3	26
2	23
3	29
3	22
1	21
3	24
2	28
13	48
5	41
3	33
5	47
4	36
7	33
2	26
3	30
1	30
2	24
2	27
5	48
2	36

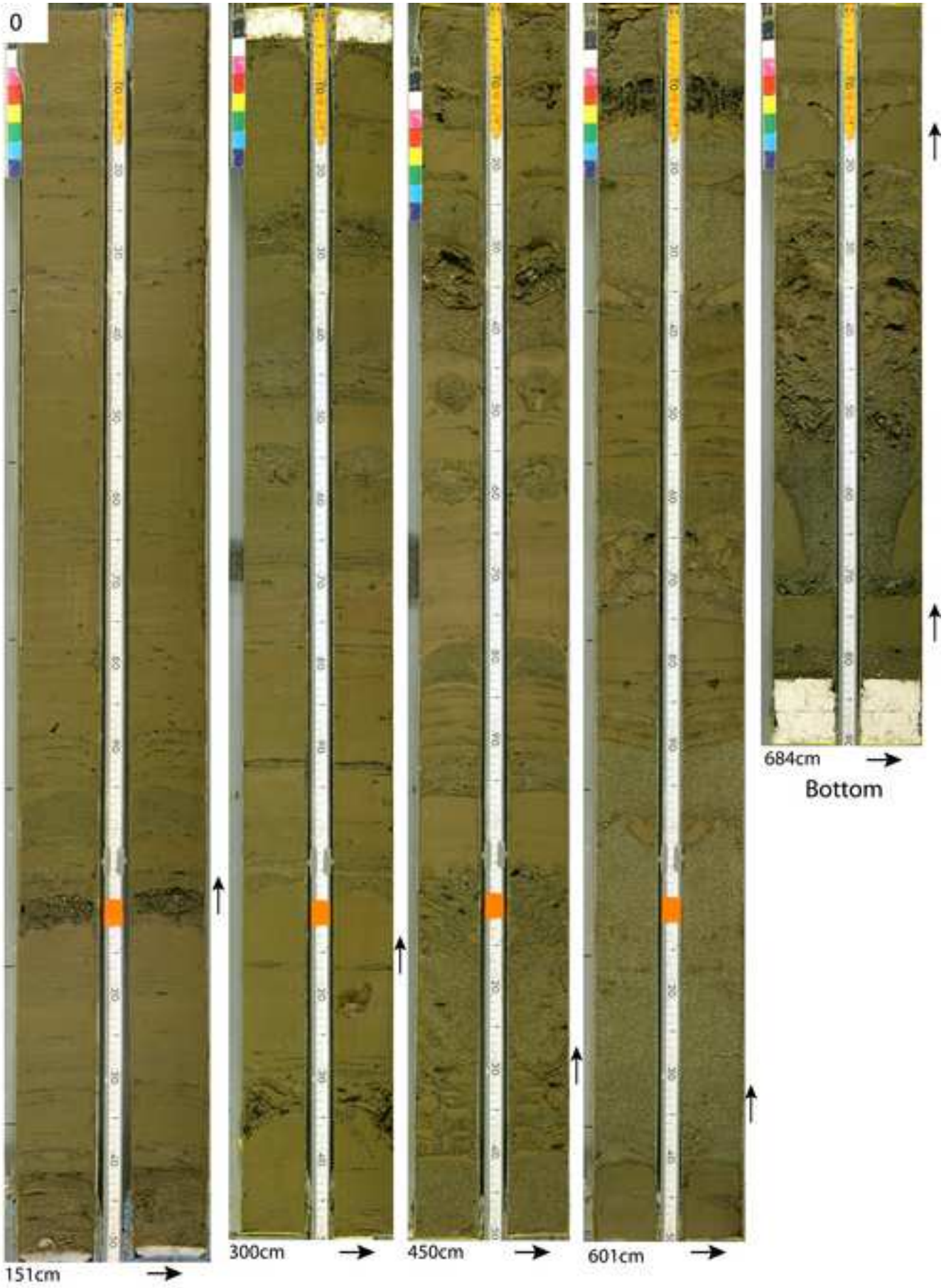

Point bar of Boreaux Nord, West part (chute channel)

Downstream marked by the arrows

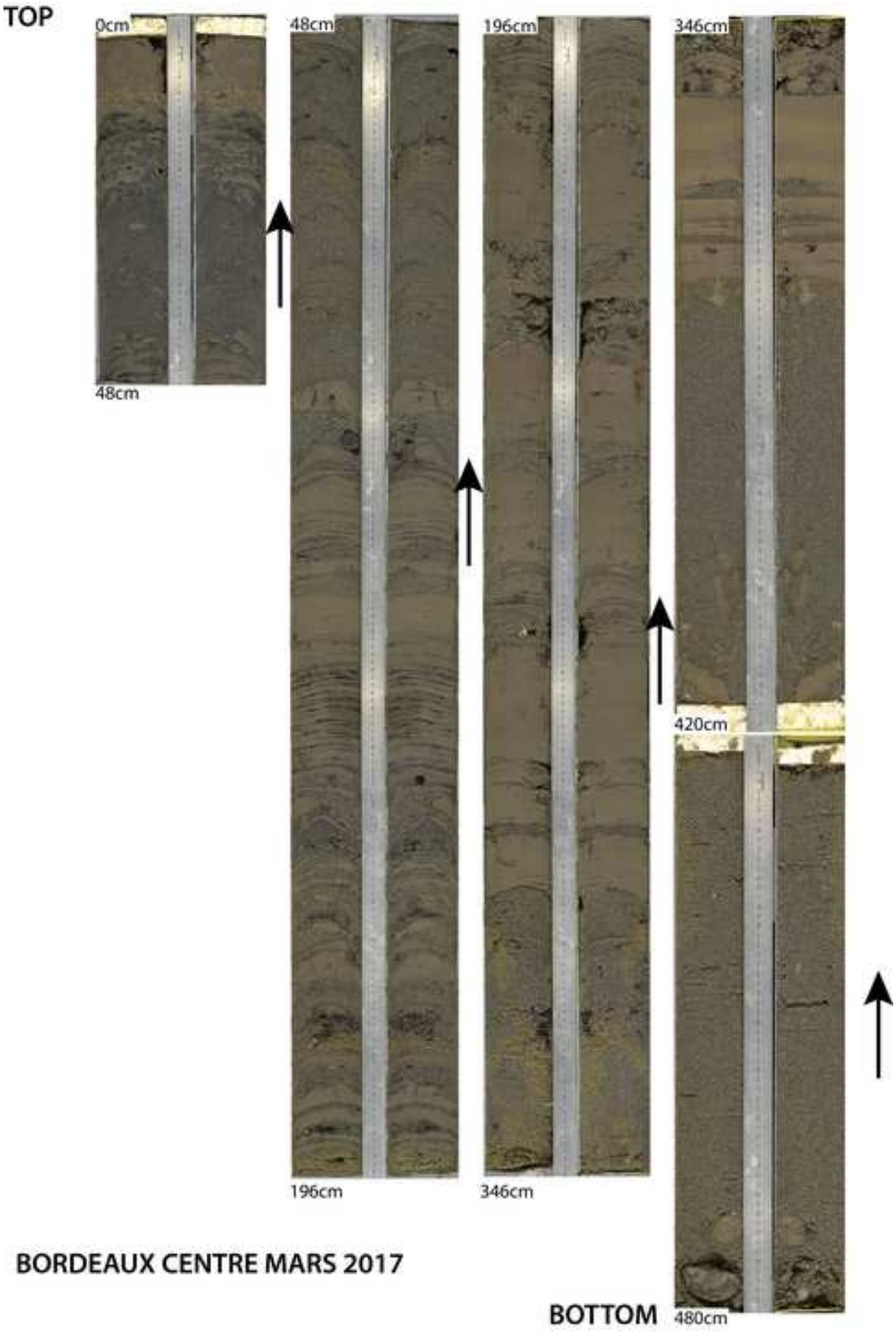

BORDEAUX CENTRE MARS 2017

Appendix 4

Click here to access/download;Appendices;Bordeaux Est.png

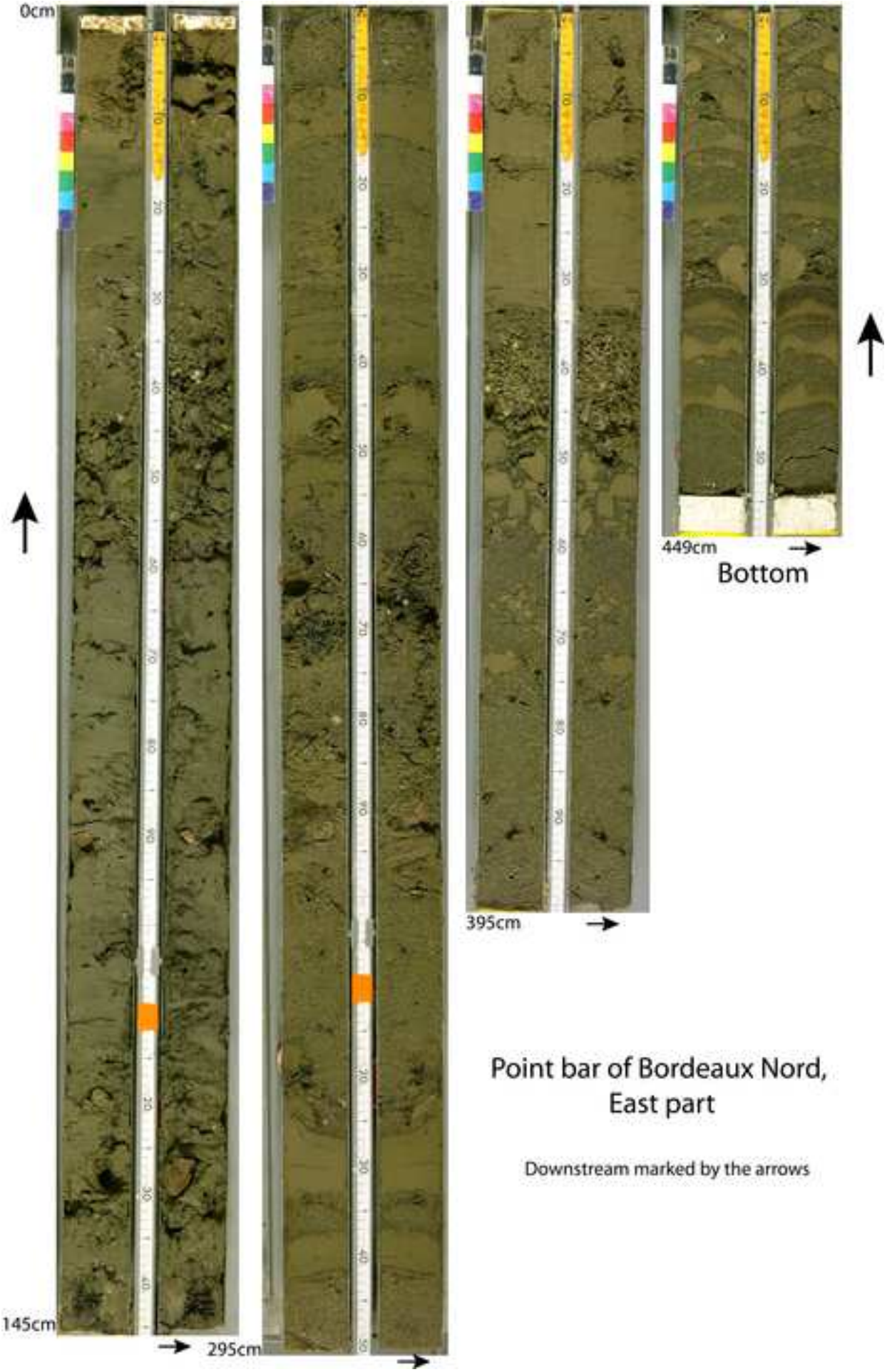

Point bar of Bordeaux Nord, East part

Downstream marked by the arrows

Bordeaux Point Bar

Click here to access/download;Potential Cover Art;DSCN9199.jpg